Electronic Supplementary Material (ESI) for Chemical Communications.
This journal is © The Royal Society of Chemistry 2022

Electronic Supplementary Information

for

Toggling the Z-Type Interaction Off-On in Nickel-Boron Dihydrogen and Anionic Hydride Complexes

Jacob R. Prat,[a] Ryan C. Cammarota,[a] Brendan J. Graziano,[a] James T. Moore,[a] and Connie C. Lu[a,b,*]

[a]Department of Chemistry, University of Minnesota, 207 Pleasant Street SE, Minneapolis, Minnesota 55455-0431, United States.
[b]Institute of Inorganic Chemistry, University of Bonn, Gerhard-Domagk-Str. 1, 53121 Bonn, Germany

*e-mail: clu@uni-bonn.de

Table of Contents

General Considerations. Unless otherwise stated, all manipulations were performed under a dinitrogen or argon atmosphere in a glovebox. Ultra-high purity gases were used when possible. Celite and molecular sieves were dried at 340 °C under vacuum. Standard solvents were deoxygenated by sparging with inert gas and dried by passing through activated alumina columns of a SG Water solvent purification system. Deuterated solvents were purchased from Cambridge Isotope Laboratories, Inc., degassed via freeze-pump-thaw cycles and stored over activated 4 Å molecular sieves. Reagents were purchased from Sigma Aldrich or Strem Chemicals. Trimethyl borate was purified by stirring with excess sodium metal under an inert atmosphere followed by vacuum distillation. Potassium *tert*-butoxide was sublimed under high-vacuum prior to use. Both $N(o\text{-}(NHCH_2P^iPr_2)C_6H_4)_3$ (abbreviated as LH_3) and Li_3NiL was prepared according to literature methods.[1,2] All other reagents were used without further purification. Elemental analyses were performed by Robertson Microlit Laboratories, Inc. (Ledgewood, NJ).

Physical Methods. ^1H and ^{31}P NMR spectra were recorded on a Bruker 400 MHz spectrometer. NMR shifts were referenced to the internal solvent residual signal (for ^1H spectra) or an external H_3PO_4 reference (for ^{31}P spectra). IR spectra were obtained in KBr pellets using a Bruker Tensor-37 FTIR spectrometer with OPUS 6.5 software. Cyclic voltammetry was conducted using a CH Instruments 600 electrochemical analyzer. The one-cell setup utilized a glassy carbon working electrode, Pt wire counter electrode, and Ag wire pseudo-reference electrode. Analyte solutions were prepared in 0.4 M $[^nBu_4N]PF_6$ in THF and referenced internally to the $FeCp_2^+/FeCp_2$ (abbreviated as Fc^+/Fc) redox couple. UV−vis spectra were collected on a Cary-300 instrument.

X-ray Crystallography and Structure Refinement Details

A yellow rod of **1-N$_2$** (0.15 × 0.15 × 0.11 mm), a red rod of **1** (0.18 × 0.18 × 0.16 mm), a yellow needle of $[(K[2.2.2]Crypt)^+][\mathbf{1}\text{-}\mathbf{H}^-]$ (0.2 × 0.1 × 0.1 mm) were mounted on a 100 μm MiTeGen microloop and placed on a Bruker PHOTON-II CMOS diffractometer for data collection at 100(2) K. The data collection was carried out using Mo Kα radiation with normal parabolic mirrors. The intensities were corrected for absorption and decay with SADABS.[3] Final cell constants were obtained from least-squares fits from all reflections. Crystal structure solution was done through intrinsic phasing (SHELXT-2014/5),[4] which provided most non-hydrogen atoms. Full matrix least-squares/difference Fourier cycles were performed using SHELXL-2016/6 and GUI ShelXle to locate the remaining non-hydrogen atoms.[5,6] All non-hydrogen atoms were refined with anisotropic displacement parameters. All non-hydride hydrogen atoms were placed in ideal positions and refined as riding atoms with relative isotropic displacement parameters. The hydride hydrogen atom of $[(K[2.2.2]Crypt)^+]\mathbf{1}\text{-}\mathbf{H}^-]$ was placed via residual electron density. The crystal structures of **1** contained heavily disordered solvent molecules. The SQUEEZE function of the PLATON program was used to remove these solvent molecules from the void space.[7] The SQUEEZE function removed 172 electrons from a void-space volume of 919 Å^3 in **1**. These values are consistent with the presence of approximately 3 hexane molecules in the unit cell of **1**.

Experimental Procedures

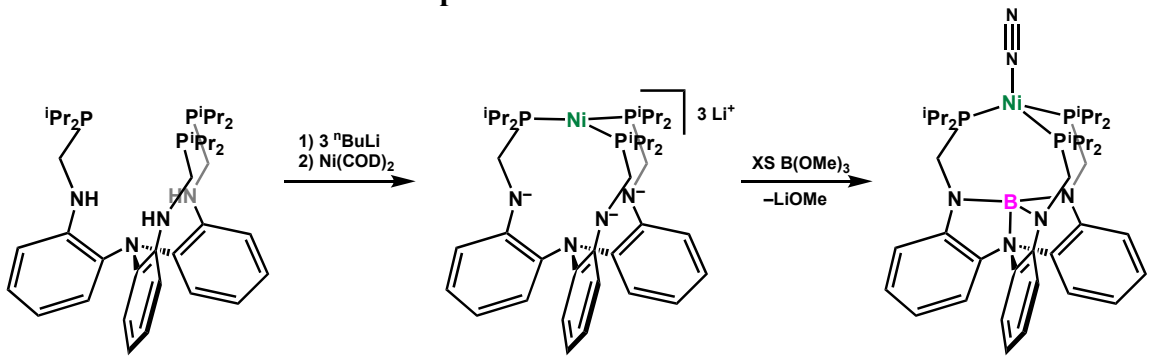

Synthesis of (N_2)NiB(N(*o*-$(NCH_2P^iPr_2)C_6H_4)_3$), 1-N_2. The entirety of this procedure was performed under an N_2 atmosphere. In a Teflon-valved bomb flask, Li_3NiL (104 mg, 137 μmol) was dissolved in ca. 15 mL 1:1 THF/toluene. To this solution was added $B(OMe)_3$ (306 μL, 2.75 mmol). The flask was then sealed and heated for 24 h at 50 °C. The solution was allowed to cool, and volatiles were removed *in vacuo*. The deep-red residue was extracted with pentane (3 x 5 mL) and filtered over Celite. The solvent was removed *in vacuo* and the residue was washed with a minimal amount of cold (–78 °C) pentane. The residue was redissolved in ca. 10 mL pentane and was bulk recrystallized via the slow evaporation of pentane into toluene. Yield: 74.5 mg, 73%. Single crystals suitable for X-ray diffraction were grown at –25 °C from a concentrated pentane solution under dinitrogen. $^1H\{^{31}P\}$ NMR (400 MHz, THF-d_8), δ: 7.52 (d, J = 7.8 Hz, 3H, aryl), 7.06 (t, J = 7.7 Hz, 3H, aryl), 6.76 (d, J = 8.1 Hz, 3H, aryl), 6.59 (t, J = 7.6 Hz, 3H, aryl), 3.52 (br, 6H, CH_2), 2.18 (m, 6H, $CHMe_2$), 1.43 (d, J = 7.2 Hz, 18H, CH_3), 1.30 (br, 18H, CH_3). $^{31}P\{^1H\}$ NMR (162 MHz, THF-d_8), δ: 23.9. ^{11}B NMR (128 MHz, THF-d_8), δ: 17 (br). IR (KBr pellet), cm^{-1}: 2065 (ν_{N2}). $C_{39}H_{60}N_6BP_3Ni$: 60.38 C, 7.80 H, 10.84 N. Found: 60.68 C, 7.72 H, 10.68 N.

Synthesis of NiB(N(*o*-$(NCH_2P^iPr_2)C_6H_4)_3$), 1. The evaporation of benzene (ca. 6 ml) from a solution of **1-N_2** (15.6 mg, 20.1 μmol) under an argon atmosphere results in the quantitative production of red **1** (14.9 mg). Single crystals suitable for X-ray diffraction were grown at –35 °C from a concentrated pentane solution under argon. $^1H\{^{31}P\}$ NMR (400 MHz, C_6D_6), δ: 7.23 (dd, J = 7.72 &1.34 Hz, 3H, Aryl), 7.05 (td, J = 784 & 1.36 Hz, 3H, Aryl), 6.72 (d, J = 8.10 Hz, 3H, Aryl), 6.50 (td, J = 7.63 & 0.9 Hz, 3H, Aryl), 3.57 (br, 6H, CH_2), 2.11 (m, 6H, $CHMe_2$), 1.44 (m 18H, CH_3), 1.17 (br, 18H, CH_3). $^{31}P\{^1H\}$ NMR (162 MHz, C_6D_6), δ: 17.1. ^{11}B NMR (128 MHz, C_6D_6), δ: 17 (br). UV−Vis [THF, λ_{max} (nm), ε ($M^{-1}cm^{-1}$)]: 520 (4800). Anal. Calcd. $C_{39}H_{60}N_4BP_3Ni$: 62.68 C, 8.09 H, 7.5 N. $C_{39}H_{60}N_4BP_3O_3Ni\bullet(C_6H_6)_{0.5}$: 60.46 C, 7.61 H, 6.71 N. Found: 60.56 C, 7.68 H, 6.93 N. Note: Lypholization from benzene was performed to produce the nitrogen free sample used for elemental analysis. A molecule of benzene per two of metal complexes retained by the sample coupled by inadvertent oxidation of the phosphines allows the sample to pass by 0.22%.

***In situ* synthesis of (H_2)NiB(N(*o*-$(NCH_2P^iPr_2)C_6H_4)_3$), 1-H_2.** A solution of **1-N_2** (5.6 mg, 7.2 μmol) in 550 μL C_6D_6 in a J-Young NMR tube was subjected to three freeze-pump-thaw cycles. To the headspace 1 atm H_2 was admitted and the tube was sealed. As the solution was allowed to thaw the color changed from a deep-red color to a clear yellow solution. $^1H\{^{31}P\}$ NMR (400 MHz, C_6D_6) δ: 7.25 (dd, J = 7.7 & 1.4 Hz, 3H, Aryl), 7.06 (td, J = 7.8 & 1.4 Hz, 3H, Aryl), 6.82 (dd, J

= 8.1 & 1.2 Hz, 3H, Aryl), 6.53 (td, J = 7.6 & 1.2 Hz, 3H, Aryl), 3.59 (s, 6H, CH_2), 1.96 (app q, J = 7.7 Hz, 6H, CH), 1.35 (app q, J = 7.2 Hz, 18H, CH_3), 1.14 (br 18H, CH_3), 0.48 (s, 2H, H_2). $^{31}P\{^1H\}$ NMR (162 MHz, C_6D_6) δ: 31.7. ^{11}B NMR (128 MHz, C_6D_6), δ: 18 (br). Due to the labile nature of the H_2 ligand, elemental analysis was not performed.

Synthesis of [K([2.2.2]-crypt)][HNiB(N(*o*-(NCH$_2$P^{i}Pr$_2$)C$_6$H$_4$)$_3$)], [(K[2.2.2]Crypt)$^+$]**1-H$^-$.** In the glovebox, **1** (31.7 mg, 42.4 μmol), [2.2.2]-cryptand (79.8 mg, 212 μmol), and potassium *tert*-butoxide (95.2 mg, 848 μmol) were dissolved in ca. 10 mL of toluene in a 50 mL Teflon-valved bomb flask. Vacuum was briefly applied to evacuate the headspace of the flask. The flask was removed from the glovebox and attached to the vacuum line where 4 atm of H_2 (the resulting pressure from cooling 1 atm H_2 with LN_2) was administered to the flask, which resulted in a color change from deep-red to red-orange. After the flask was left sealed at this pressure for 3 days, the solution was frozen with liquid nitrogen. Separately, a Teflon-valved bomb flask of hexanes was degassed via three freeze-pump-thaw cycles and was saturated with H_2. Approximately 40 mL of hexanes was cannula transferred via an overpressure of H_2 creating a layer over the toluene solution. The entire solution was frozen, 4 atm of H_2 was administered, and the vessel was sealed. After a week small yellow-orange XRD quality needles were apparent. The mother-liquor was removed and the flask was dried under vacuum. The crystals were washed with hexanes, and extracted and filtered with ca. 10 mL DME to give an orange residue. Yield: 30.6 mg, 62%. The deuteride isotopologue was synthesized in an analogous manner, only using D_2 in the place of H_2. $^1H\{^{31}P\}$ NMR (400 MHz, THF) δ 6.79 (d, J = 5.9 Hz, 3H, Aryl), 6.50 (m, 6H, Aryl), 6.14 (td, J = 7.0 & 2.1 Hz, 3H, Aryl), 3.56 (s, 12H, Cryptand (OC*H*$_2$)$_2$), 3.52 (t, J = 4.6 Hz, 12H, Cryptand OC*H*$_2$CH$_2$N), 3.44 (d, J = 9.5 Hz, 3H, C*H*H′), 2.92 (d, J = 10.6 Hz, 3H, CH*H*′), 2.53 (t, J = 4.7 Hz, 12H, Cryptand OCH$_2$*CH*$_2$N), 1.96 (app p, J = 7.3 Hz, 3H, C*H*Me$_2$), 1.64 (sept, J = 7.4 Hz, 3H, C*H*Me$_2$), 1.43 (d, 9H, J = 7.41 Hz, ^{i}Pr CH$_3$), 1.26 (d, J = 7.23 Hz, 9H, ^{i}Pr CH$_3$), 1.12 (d, J = 7.7 Hz, 9H, ^{i}Pr CH$_3$), 0.79 (d, J = 6.93 Hz, 9H, ^{i}Pr CH$_3$), –8.26 (1:1:1:1 q, $^2J_{B–H}$ = 25.5 Hz, 1H, NiH).$^{31}P\{^1H\}$ NMR (162 MHz, THF) δ 58.73 (s). ^{11}B NMR (128 MHz, THF) δ 22.67 (d, $^2J_{B–H}$ = 25.9 Hz). Multiple combustion analysis attempts were made. The reactive nature of the complex likely hindered measurement due to inadvertent decomposition.

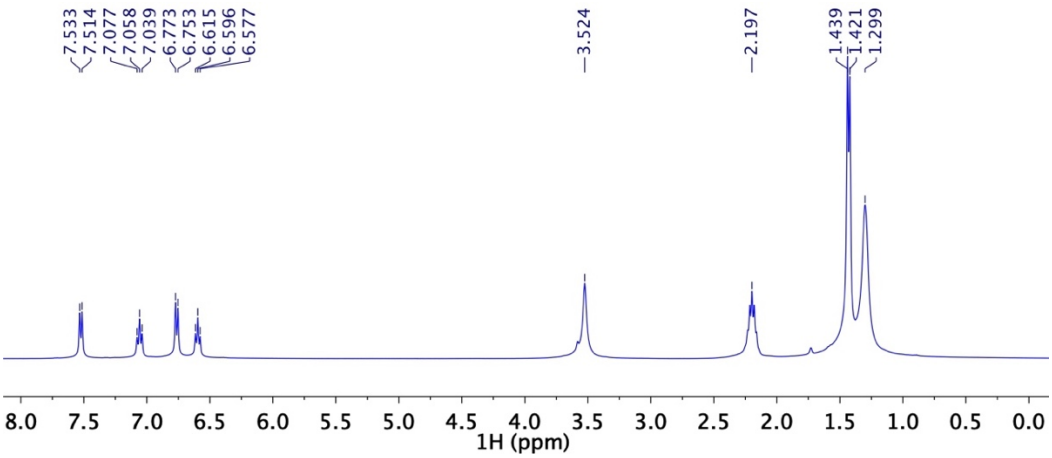

Figure S1: $^{1}H\{^{31}P\}$ NMR spectrum (400 MHz, C_6D_6) of **1-N₂**.

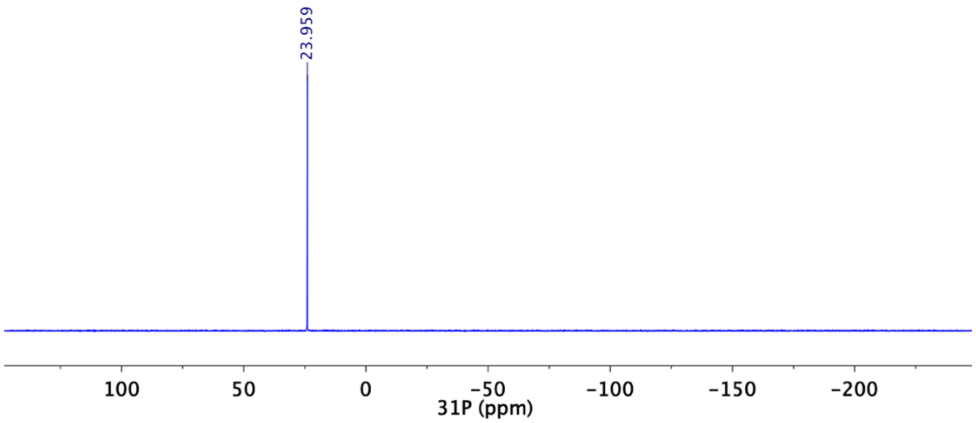

Figure S2: $^{31}P\{^{1}H\}$ NMR spectrum (162 MHz, C_6D_6) of **1-N₂**.

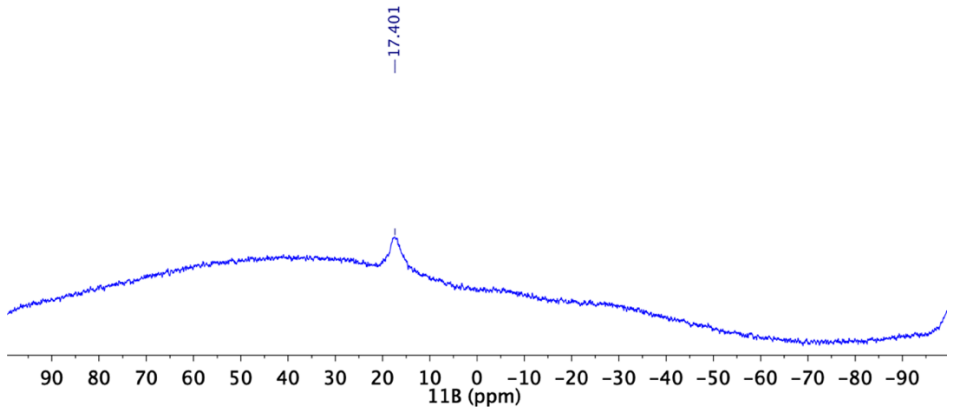

Figure S3: ^{11}B NMR spectrum (128 MHz, C_6D_6) of **1-N₂**.

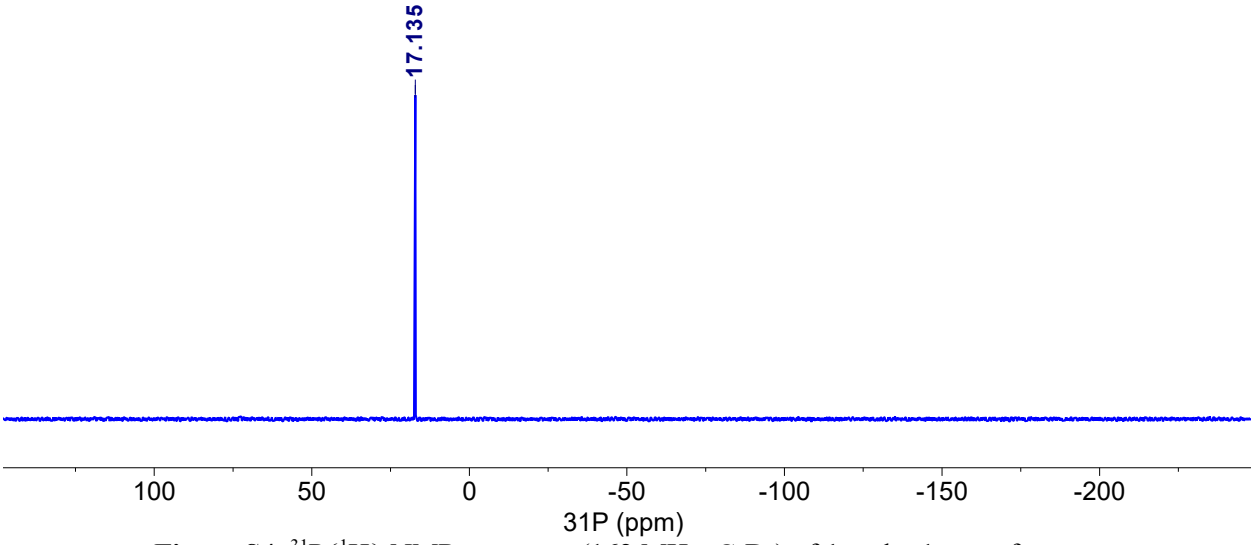

Figure S4: $^{31}P\{^{1}H\}$ NMR spectrum (162 MHz, C_6D_6) of **1** under 1 atm of argon.

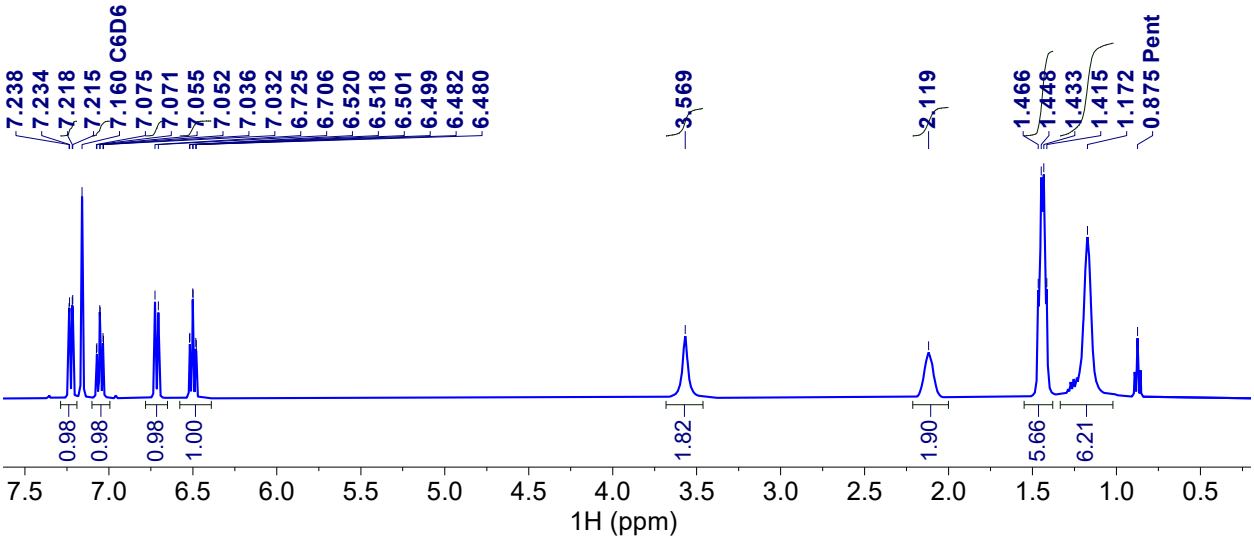

igure S5: ^{1}H NMR spectrum (400 MHz, C_6D_6) of **1** under 1 atm of argon.

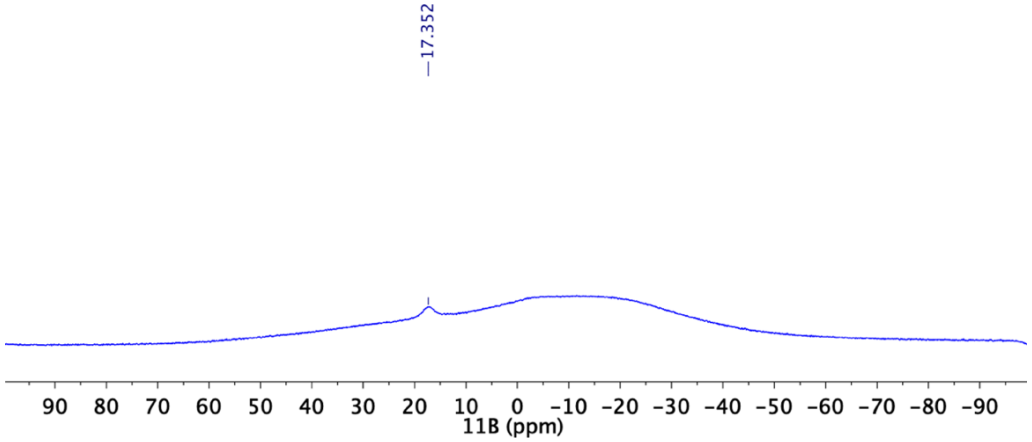

Figure S6: ^{11}B NMR spectrum (128 MHz, C_6D_6) of **1** under 1 atm of argon.

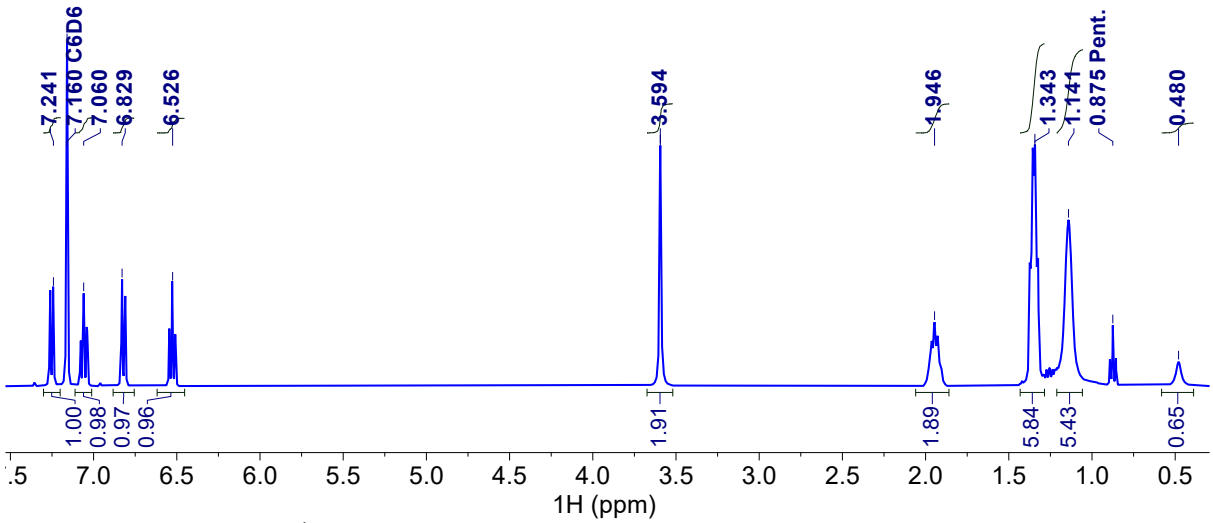

Figure S7: ^{1}H NMR spectrum (400 MHz, C_6D_6) of **1-H$_2$** under 1 atm of H_2.

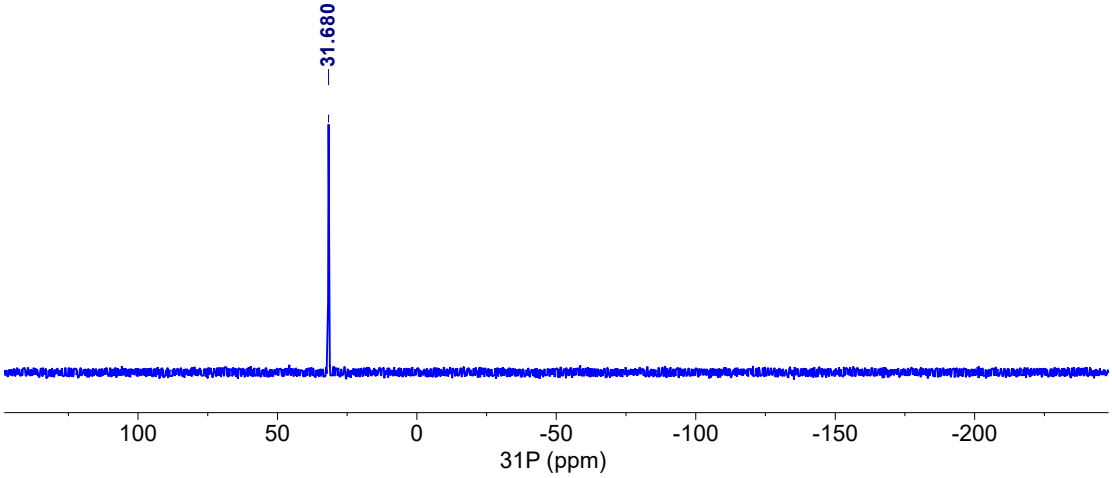

Figure S8: ^{31}P{^{1}H} NMR spectrum (162 MHz, C_6D_6) of **1-H$_2$** under 1 atm of H_2.

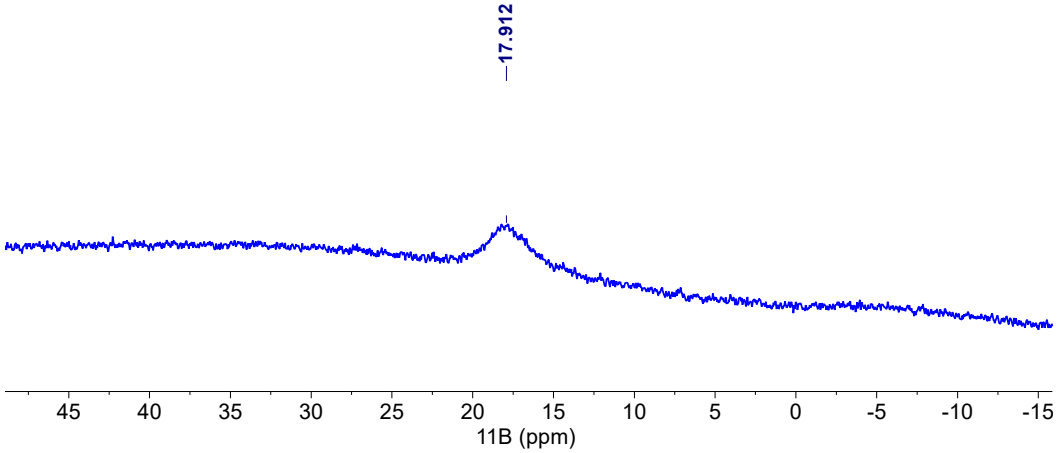

Figure S9: ^{11}B NMR spectrum (128 MHz, C_6D_6) of **1-H$_2$** under 1 atm of H_2.

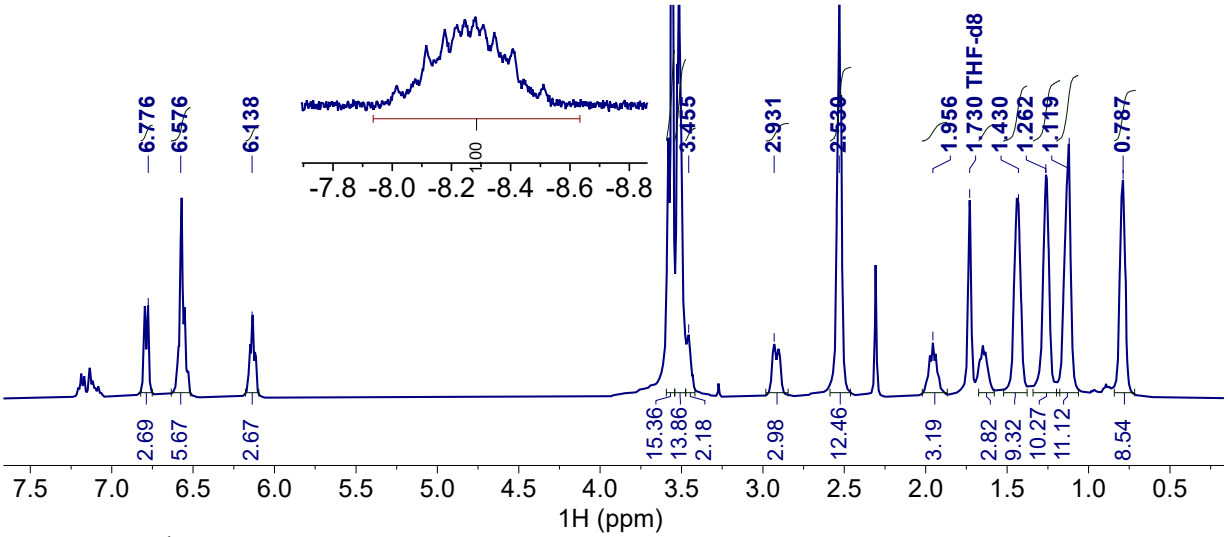

Figure S10: ^{1}H NMR spectrum (400 MHz, THF-d_8) of [(K[2.2.2]Crypt)$^{+}$]**1-H**$^{-}$. Note the signals at 7.2 and 2.3 ppm correspond to a co-crystallized toluene.

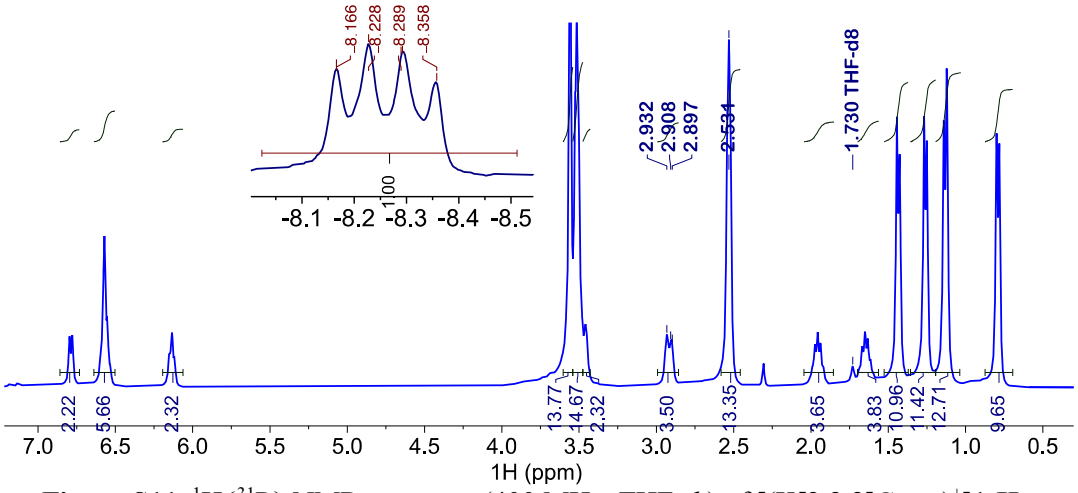

Figure S11: ^{1}H{^{31}P} NMR spectrum (400 MHz, THF-d_8) of [(K[2.2.2]Crypt)$^{+}$]**1-H**$^{-}$.

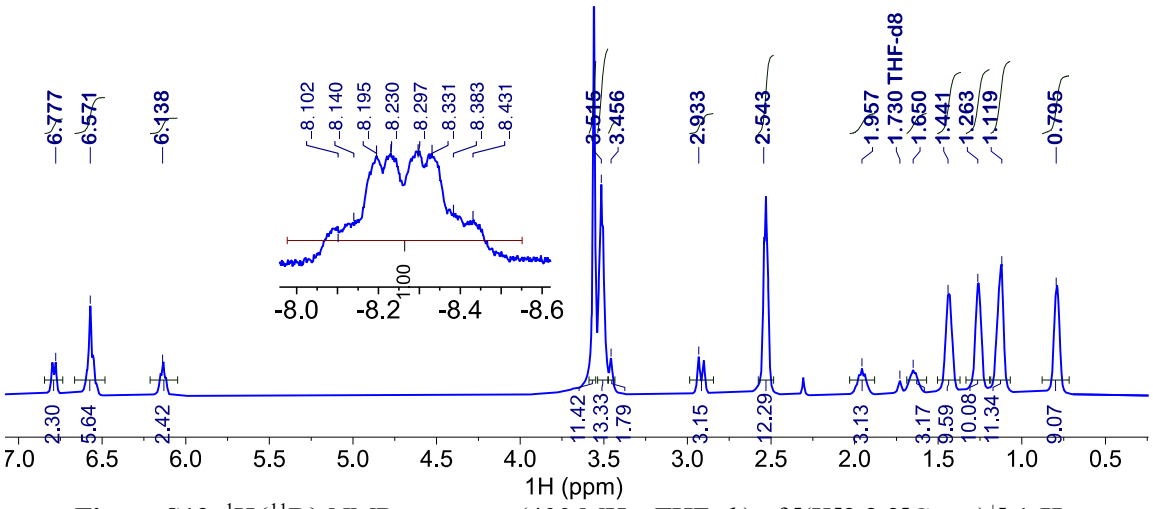

Figure S12: ^{1}H{^{11}B} NMR spectrum (400 MHz, THF-d_8) of [(K[2.2.2]Crypt)$^{+}$] **1-H**$^{-}$.

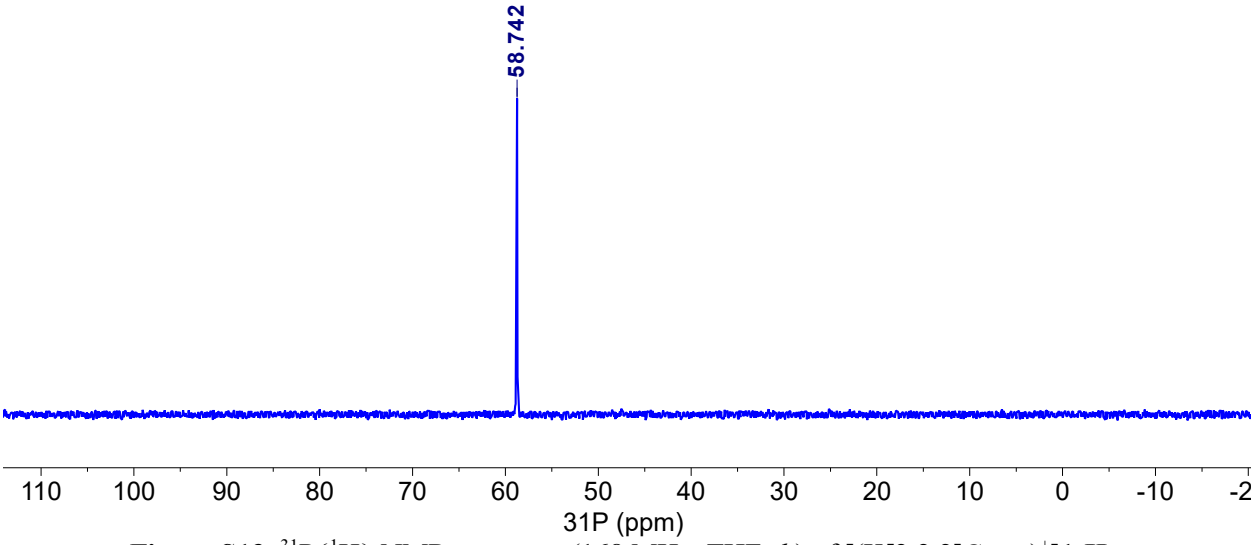

Figure S13: $^{31}P\{^{1}H\}$ NMR spectrum (168 MHz, THF-d_8) of [(K[2.2.2]Crypt)$^+$]**1-H**$^-$.

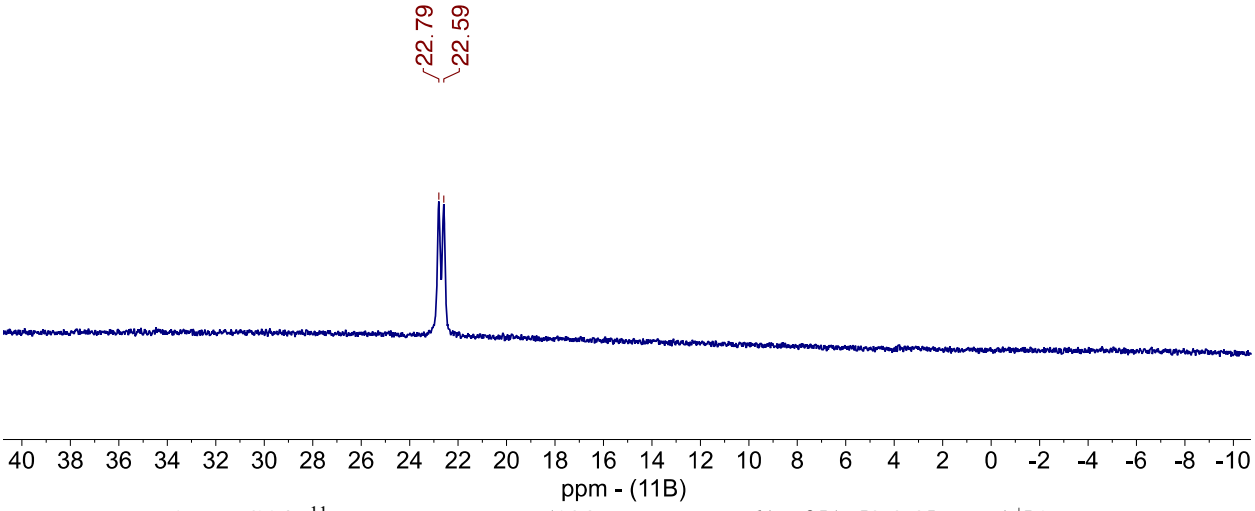

Figure S14: ^{11}B NMR spectrum (128 MHz, THF-d_8) of [(K[2.2.2]Crypt)$^+$]**1-H**$^-$.

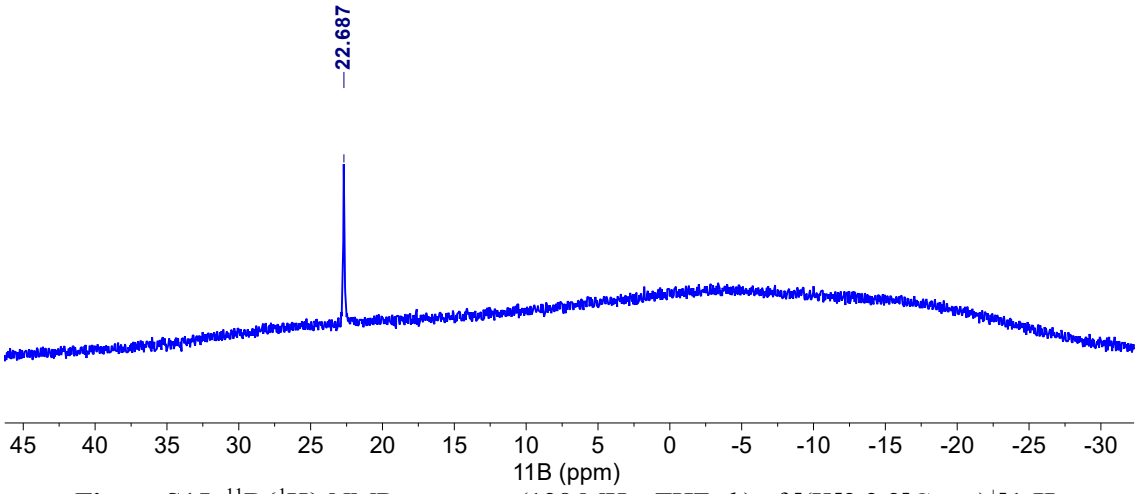

Figure S15: $^{11}B\{^{1}H\}$ NMR spectrum (128 MHz, THF-d_8) of [(K[2.2.2]Crypt)$^+$]**1-H**$^-$

Table S1: Crystallographic metrics for **1**, **1-N_2**, and **1-H^-**.

Metric	**NiBL 1**	**N_2NiBL 1-N_2**	**[K(2.2.2-Crypt)] HNiBL 1-H^-**
CCDC Deposit Number	2132870	2132872	2132871
Chemical Formula	$C_{39}H_{60}BN_4NiP_3$	$C_{39}H_{60}BN_6NiP_3$	$C_{57}H_{97}BKN_6NiO_6P_3$ C_7H_8
FW	747.34	775.36	1163.79
Temperature (K)	100(2)	100(2)	125(2)
Crystal System	Trigonal	Monoclinic	Monoclinic
Space Group	$P\bar{3}c1$	$P2_1/n$	$P2_1/n$
a (Å)	14.9296(11)	16.6281(5)	16.9341(14)
b (Å)	14.9296(11)	13.0544(5)	22.9728(19)
c (Å)	23.2119(18)	18.4221(7)	18.7504(13)
α (°)	90	90	90
β (°)	90	93.0200(10)	112.891(2)
γ (°)	120	90	90
Volume (Å^3)	4480.6(7)	3993.3(2)	6719.9(9)
Z	4	4	4
Density (g/cm^3)	1.108	1.290	1.150
μ (mm^{-1})	0.569	0.642	0.469
λ (Å)	0.71073	0.71073	0.71073
θ (°)	2.358 to 26.723	2.214 to 28.332	2.129 to 28.344
Total Reflections	49173	35413	107823
Unique Reflections	3168	9903	16747
Data/Restraints/Parameters	3168 / 0 / 149	9903 / 0 / 463	16747 / 0 / 705
R_1, $wR_2(I>2\sigma(I))$	0.0344, 0.0754	0.0455, 0.0792	0.0458, 1065

Table S2: Selected torsion metrics and geometric indices[26–28] for **1**, **1-N_2**, and **1-H^-**.

Angle (°)	**1**	**1-N_2**	**1-H^-**
Ni-P-N/P-N-B Planes 1	4.88	11.67	27.53
Ni-P-N/P-N-B Planes 2	–	8.97	27.66
Ni-P-N/P-N-B Planes 3	–	10.12	27.51
Avg.	4.88	10.25	27.57
B-N-C-P Torsion 1	78.03	82.31	2.54
B-N-C-P Torsion 2	–	80.77	17.73
B-N-C-P Torsion 3	–	74.21	11.24
Avg.	78.03	79.10	10.50
P-Ni-B-N Torsion 1	3.90	8.63	34.52
P-Ni-B-N Torsion 2	–	6.78	34.61
P-Ni-B-N Torsion 3	–	7.53	34.35
Avg.	3.90	7.65	34.49
τ_4/τ_4'	–	0.97/0.97	–
τ_5	–	–	0.99

Table S3: Crystallographic bond metrics (Å) and angles (°) for **1**, **1-N_2**, and **1-H^-**.

Metric	1	1-N_2	1-H^-
Ni–B	3.380(4)	3.735(3)	2.235(2)
Avg. Ni–P	2.1381(5)	2.2065(5)	2.1451(5)
Ni–P1	–	2.199(1)	2.1328(6)
Ni–P2	–	2.204(3)	2.1501(6)
Ni–P3	–	2.199(1)	2.1523(6)
Avg P–Ni–P	117.251(9)	109.67(4)	117.97(3)
P1–Ni–P2	–	109.57 (3)	118.64(2)
P2–Ni–P3	–	111.51(3)	117.64(2)
P1–Ni–P3	–	107.93(3)	117.72(2)
Ni–P_3 Plane	0.3583(6)	0.7280(5)	0.3057(4)
Avg. B–N_{Amide}	1.5322(16)	1.527(6)	1.576(3)
B–N1	–	1.527(3)	1.5713(27)
B–N2	–	1.529(3)	1.5757(27)
B–N3	–	1.525(3)	1.5833(27)
Avg. N_{Amide}–B–N_{Amide}	117.26(7)	117.06(3)	111.56(2)
N1–B–N2	–	118.48(2)	111.56(15)
N2–B–N3	–	115.9(2)	112.65(15)
N1–B–N3	–	116.81(2)	111.87(16)
B–N_{Apical}	1.702(4)	1.682(3)	2.803(5)
B–N_3 Plane	–0.2590(35)	–0.2646(29)	0.4552(22)
N_2–Ni–P1	–	107.44(7)	–
N_2–Ni–P2	–	108.67(7)	–
N_2–Ni–P3	–	111.57(7)	–
Ni–N_2	–	1.820(9)	–
N–N	–	1.116(5)	–
B–Ni–H	–	–	188.64(2)
Ni–H	–	–	1.56(2)

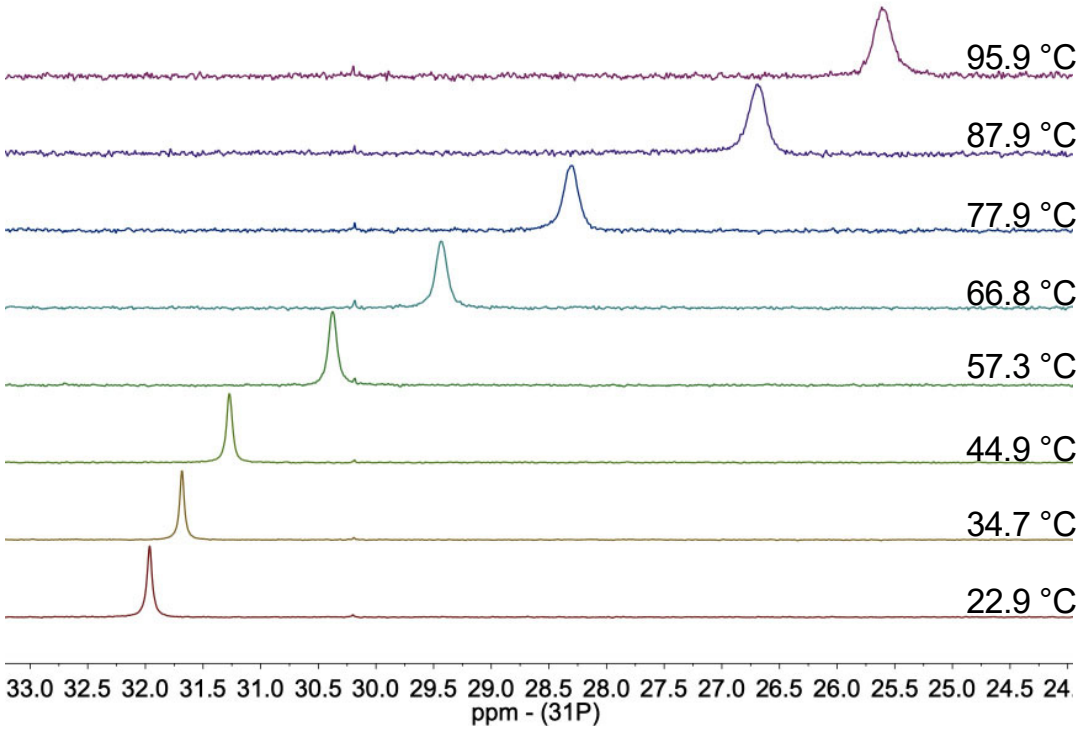

Figure S16: Variable temperature $^{31}P\{^{1}H\}$NMR spectra (128 MHz, toluene-d_8) of a 14.6 mM solution of **1-H₂** under 1 atm H_2.

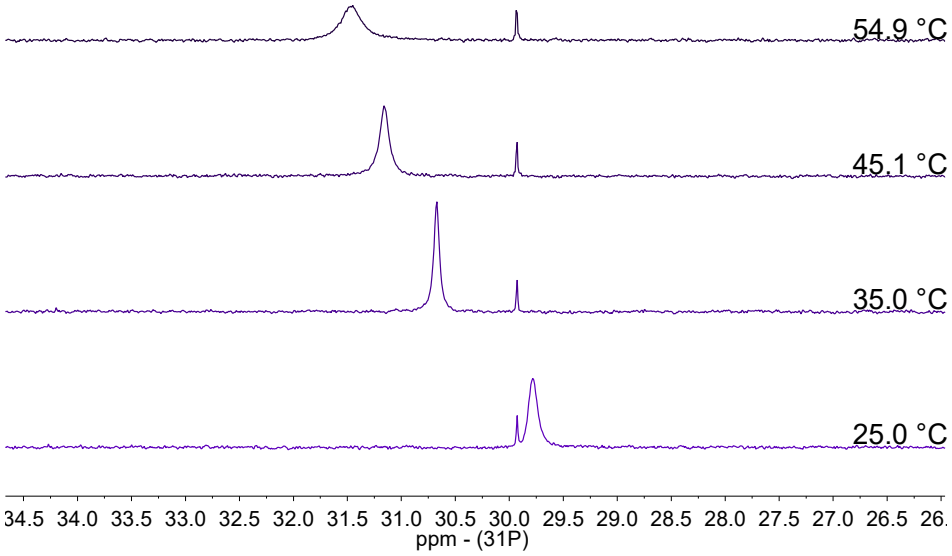

Figure S17: Variable temperature $^{31}P\{^{1}H\}$ NMR spectra (128 MHz, THF-d_8) of 15.4 mM solution of **1-H₂** under 1 atm H_2.

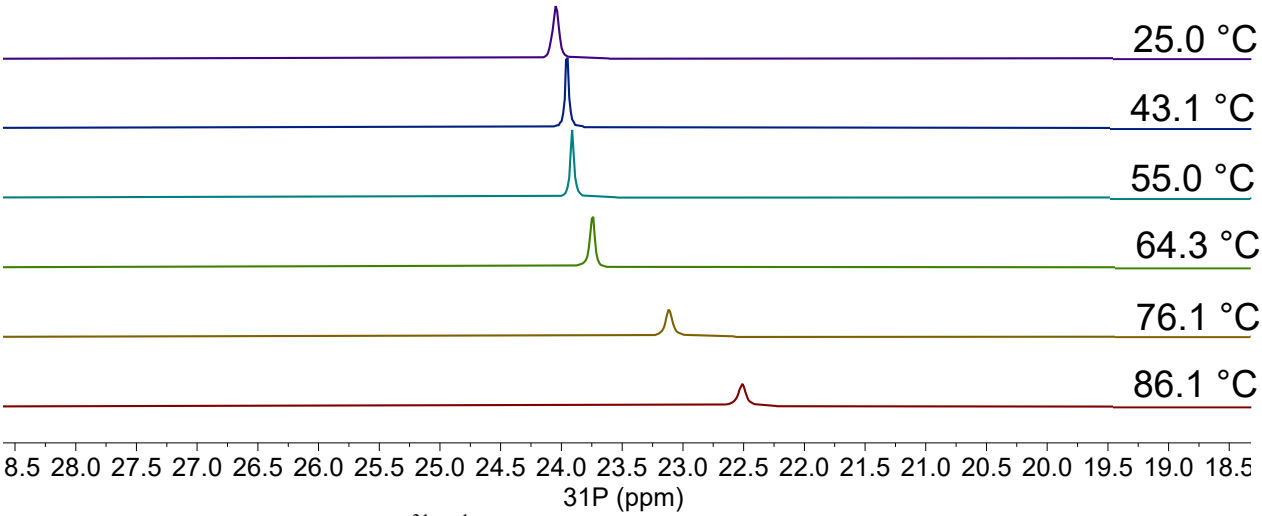

Figure S18: Variable temperature $^{31}P\{^{1}H\}$ NMR spectrum (128 MHz, toluene-d_8) of 10.5 mM solution of **1-N$_2$** under 1 atm N_2.

Determination of K_{H2} via ^{31}P NMR spectra

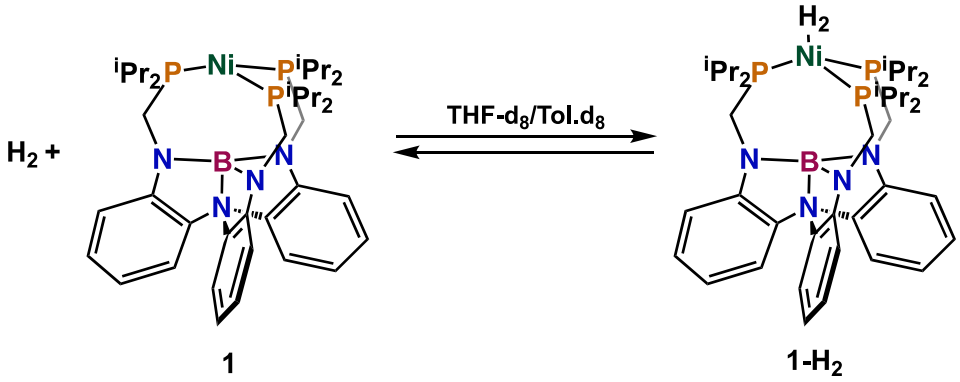

Figure S19: The equilibria between **1** and **1-H₂**.

As done previously,[12] the value of K_{H2} was calculated by using the equation 1, where X is a gaseous ligand. The values used where 31.4 ppm is the observed average shift at room temperature of **1-H₂** in THF-d_8 under 1 atm H_2, 32.1 is the shift of **1-H₂** measured under 4 atm H_2 at −65 °C, and 15.8 is the shift of **1** measured at room temperature under Ar.

$$\boldsymbol{K_{H_2}} = \frac{[(X)NiML]}{[NiML]\,P(X)} = \frac{\delta_{obs}-\delta_{NiML}}{\delta_{(X)NiML}-\delta_{obs}} \bullet \frac{1}{P(X)} \qquad \text{(S1)}$$

The concentration of the gaseous ligand, as represented as P(X), can either be expressed as the known pressure of the gas or through the empirically-determined gas concentration in organic solvents.[13,14]

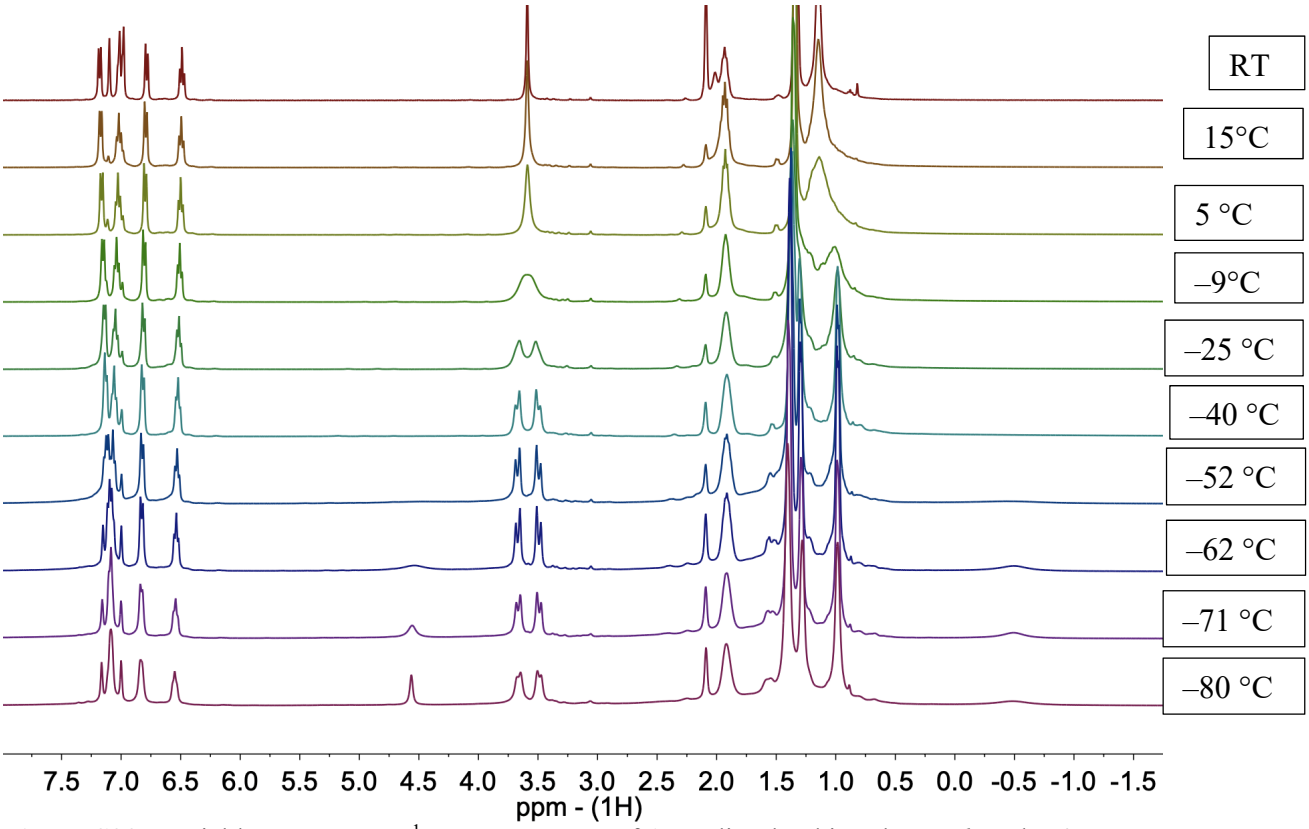

Figure S20: Variable temperature ^{1}H NMR spectra of **1-H$_2$** dissolved in toluene-d_8 under 4 atm H_2.

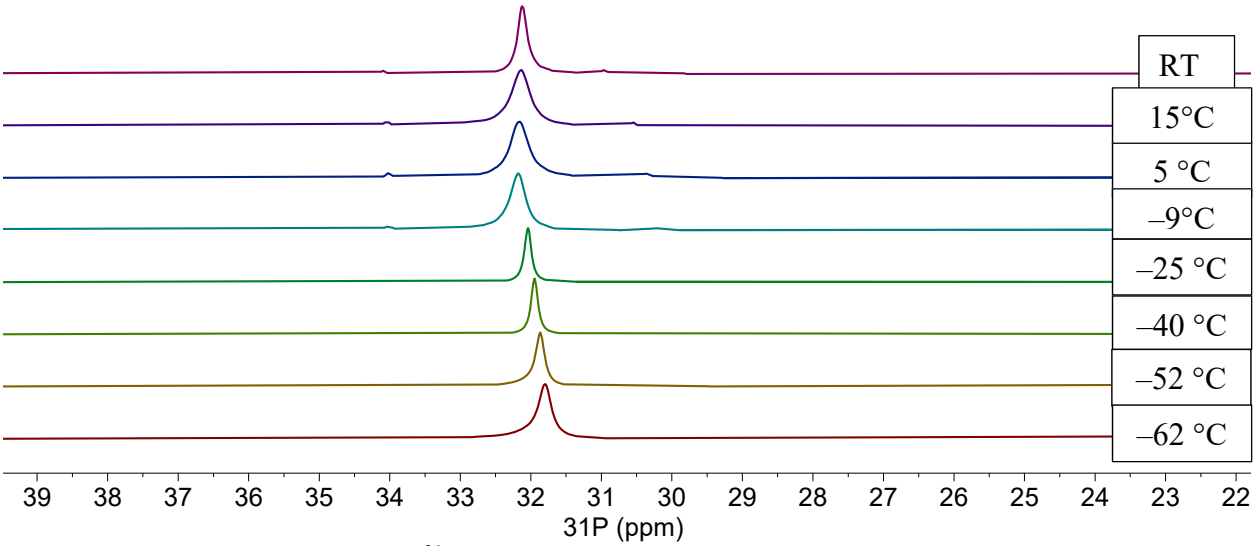

Figure S21: Variable temperature ^{31}P NMR spectra of **1-H$_2$** dissolved in toluene-d_8 under 4 atm H_2. The chemical shift measured at 4 atm and RT was used to assign the shift of **1-H$_2$**.

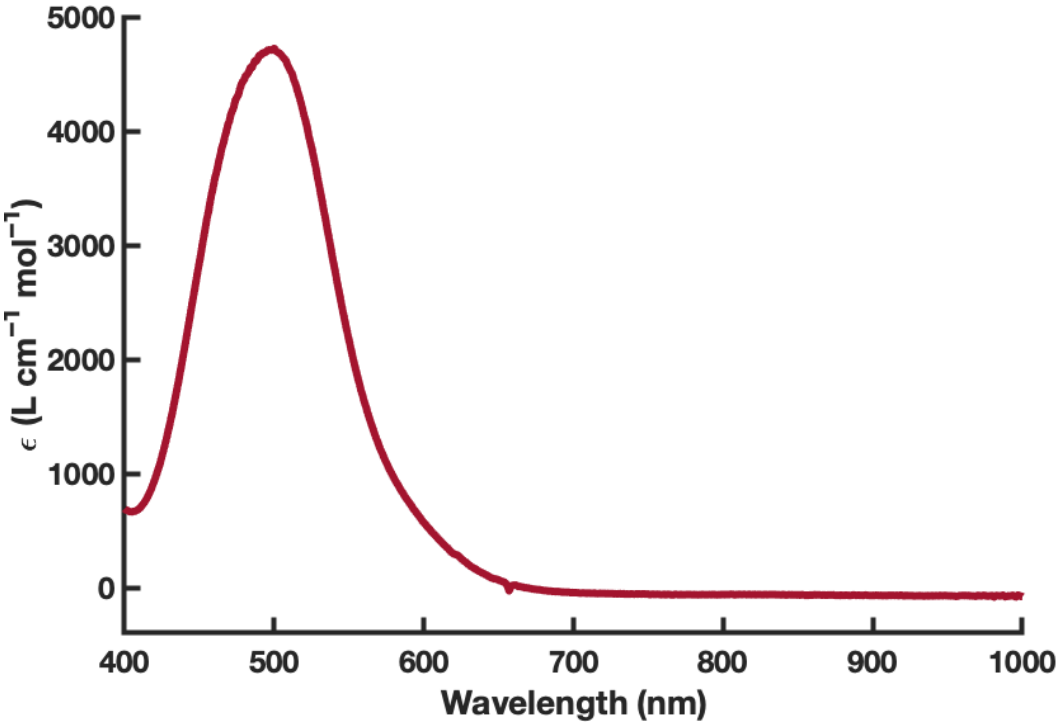

Figure S22: UV-Vis spectra of **1** under in THF under 1 atm Ar. THF, λ_{max} (nm), ε ($M^{-1}cm^{-1}$)]: 520 (4800).

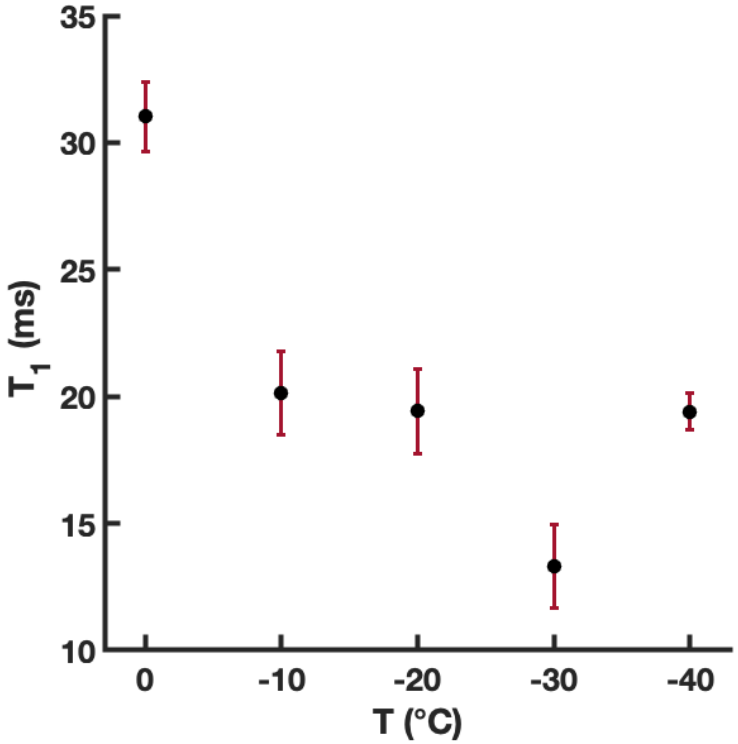

Figure S23: Variable temperature ^{1}H NMR (400 MHz, THF-d_8) T_1 determination of the hydrogen ligand of **1-H$_2$** under 1 atm H_2.

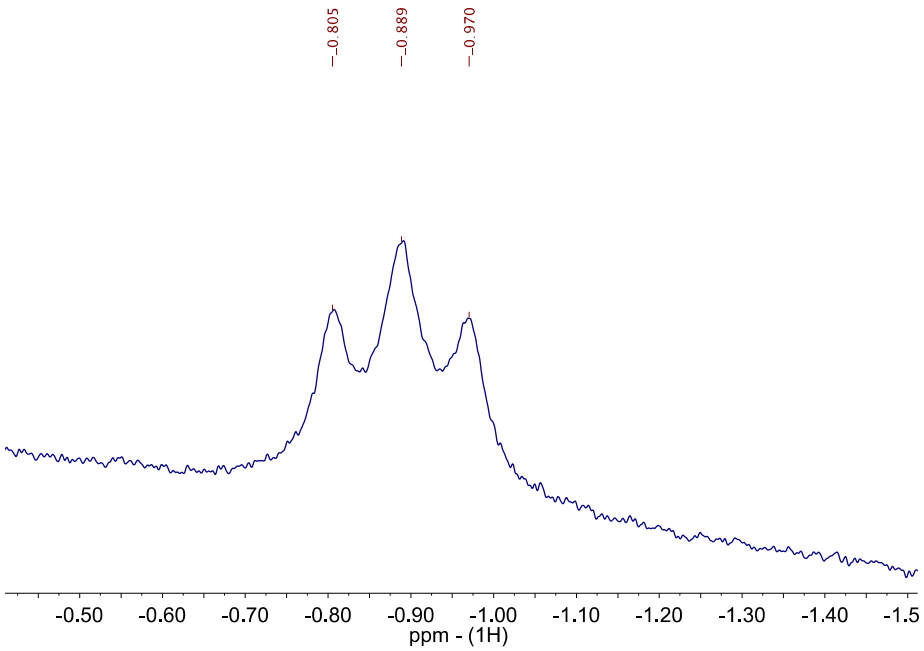

Figure S24: ^{1}H NMR spectrum (400 MHz, THF-d_8) of 14.4 mM solution of **1** under 1 atm HD. Zoom of the hydride region showing J_{HD} of 33 Hz.

The relation of bond activation of an HD ligand is reflected in the magnitude of the coupling constant (J_{HD}) of the signal in the ^{1}H NMR with the limiting case of a non-intact H–D bond (i.e. a classical dihydride) resulting in no significant coupling. A deviation from 43 Hz found for free HD gas indicates an activation of the bond, increasing the bond length from the 0.74 Å in the free gas. Both Morris and Heinekey have determined relationships for this correlation.[8]

$$d_{\mathrm{HH}}[\mathrm{Morris}] = 1.42 - 0.0167 \cdot J_{\mathrm{HD}}$$

$$d_{\mathrm{HH}}[\mathrm{Heinekey}] = 1.44 - 0.0168 \cdot J_{\mathrm{HD}}$$

Utilizing the lowest ^{1}H relaxation rates (T_1(min)) for the H_2 unit, a bond length can determined. Whether the rotation of the hydrogen ligand about the H_2–M bond is fast or static relative to the molecular tumbling in solution produces two possible limiting cases for the calculation of the H_2 bond length. The relationship between the bond length (d_{HH}), the relaxation rate (T_1(min)), and the spectrometer frequency (υ) is shown below. To convert between a fast rotation or static case a constant can be used (C = 0.793).[9–11] As shown in Table S4, the fast timescale aligns with the values calculated from the observed J_{HD}.

$$\mathrm{d_{HH}(fast)} = 5.81 \cdot \sqrt[6]{T_1(\mathrm{min})/(4\upsilon)}$$

$$d_{\mathrm{HH}}(\mathrm{static}) = \frac{d_{\mathrm{HH}}}{C}$$

Table S4: Comparison of the H_2 activation parameters for the H_2 or HD adducts of the NiML series, where M = B (**1**), Al (**2**), Ga (**3**), and In (**4**). Pressure is 1 atm unless otherwise specified.

Metric	1	2	3	4
J_{HD}, Hz	33	34.4[a]	33.2	32
T_1(min), ms	13(2)[b]	≤ 49(5)[c]	≤ 16(6)[d]	23(5)[d]
$d_{H\text{-}H}$ from J_{HD}, Å *Heinekey*	0.88	0.86	0.88	0.91
$d_{H\text{-}H}$ from T_1(min) *fast*	0.83	≤ 0.99[c]	≤ 0.80(5)	0.85(3)

[a]3.8 atm. [b]400 MHz. [c]500 MHz, 34 atm. [d]600 MHz. See reference 12 for more details.

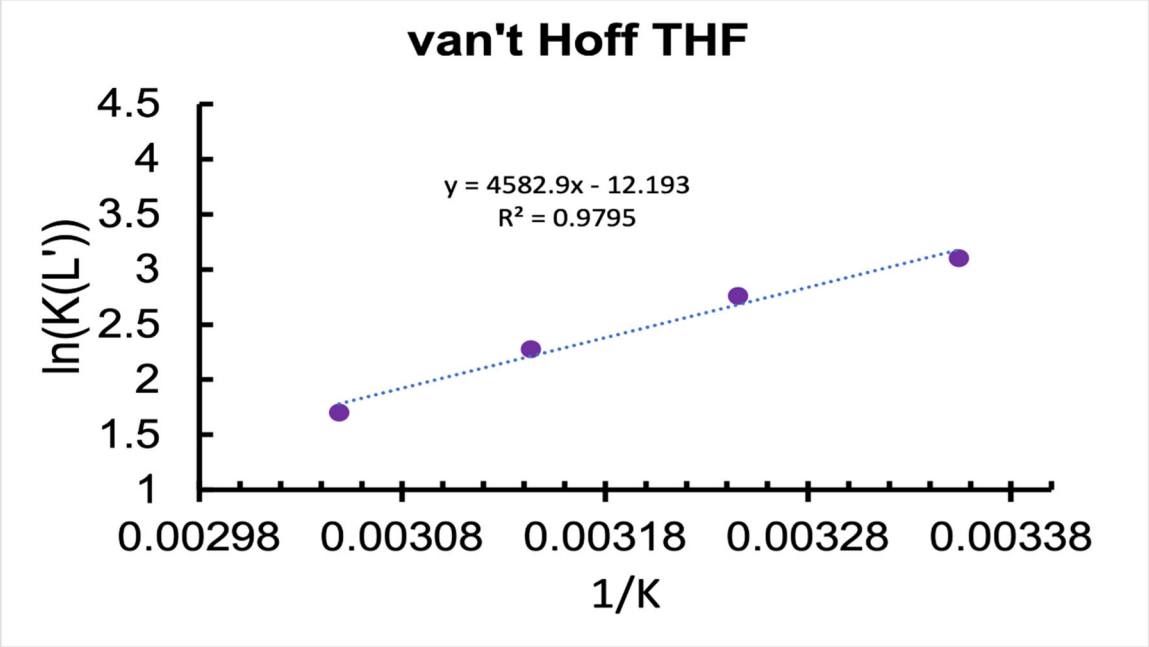

Figure S25: The van't Hoff plot of **1-H₂** from the NMR spectrum in THF-d_8 at elevated temperatures.

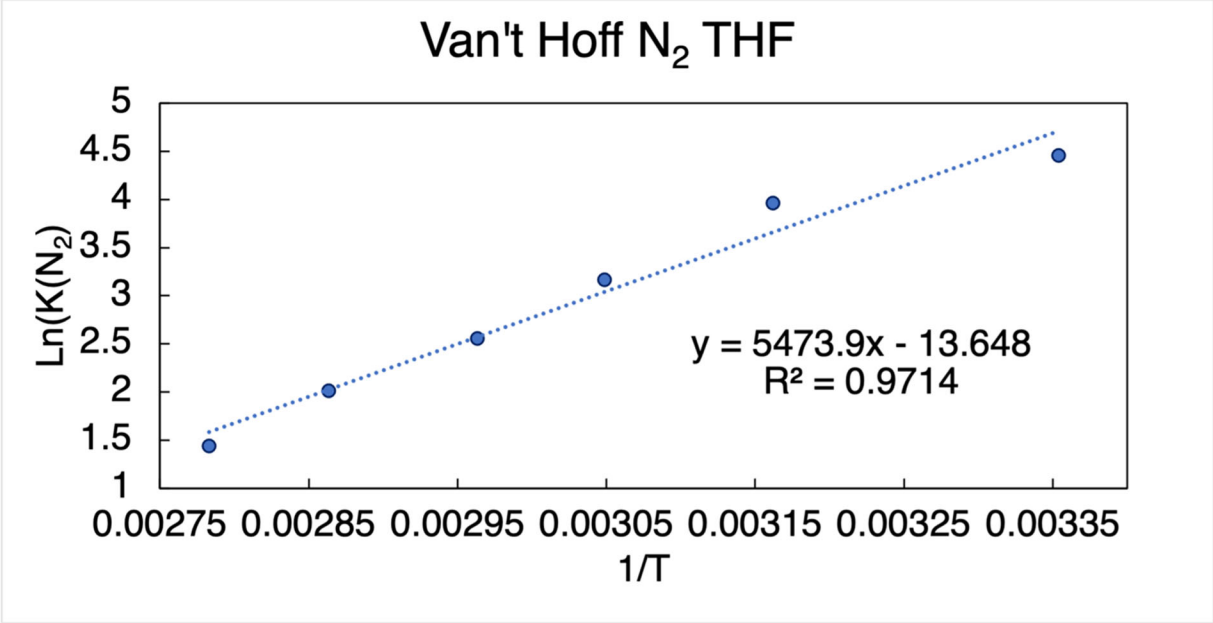

Figure S26: The van't Hoff plot of **1-N_2** from the NMR spectrum in toluene-d_8 at elevated temperatures.

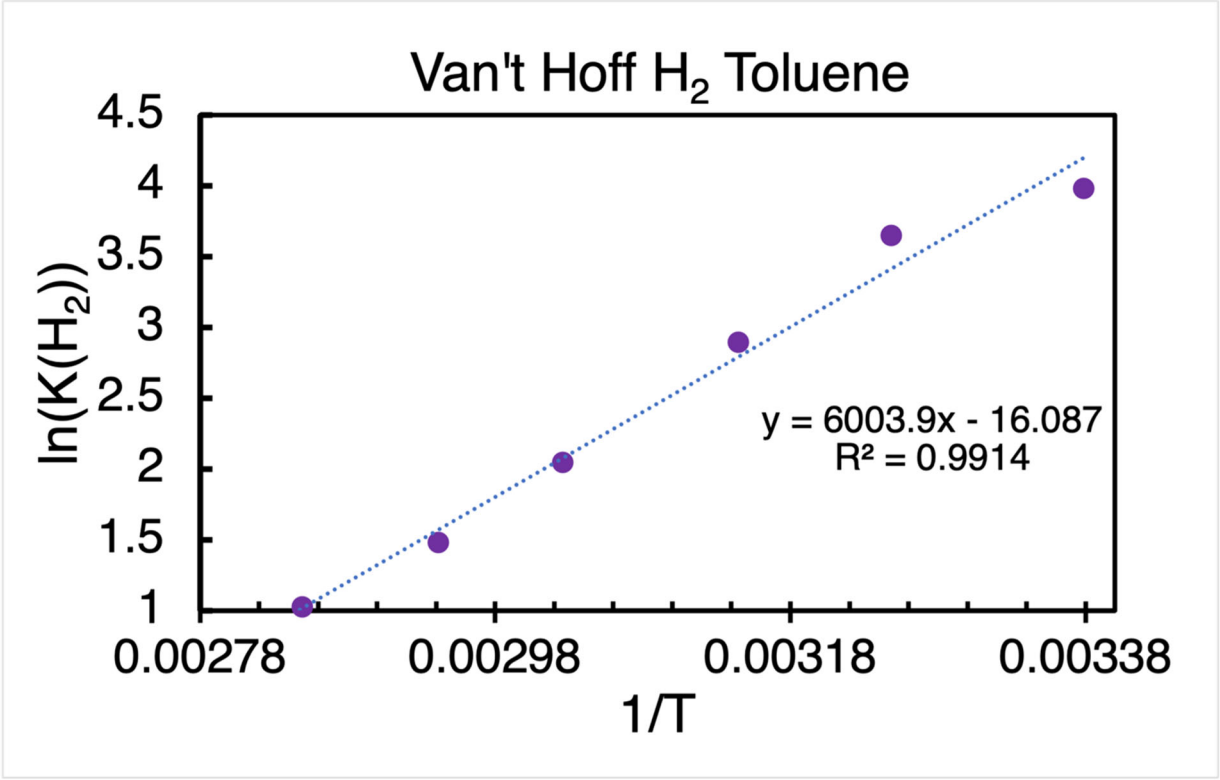

Figure S27: The van't Hoff plot of **1-H_2** from the NMR spectrum in toluene-d_8 at elevated temperatures.

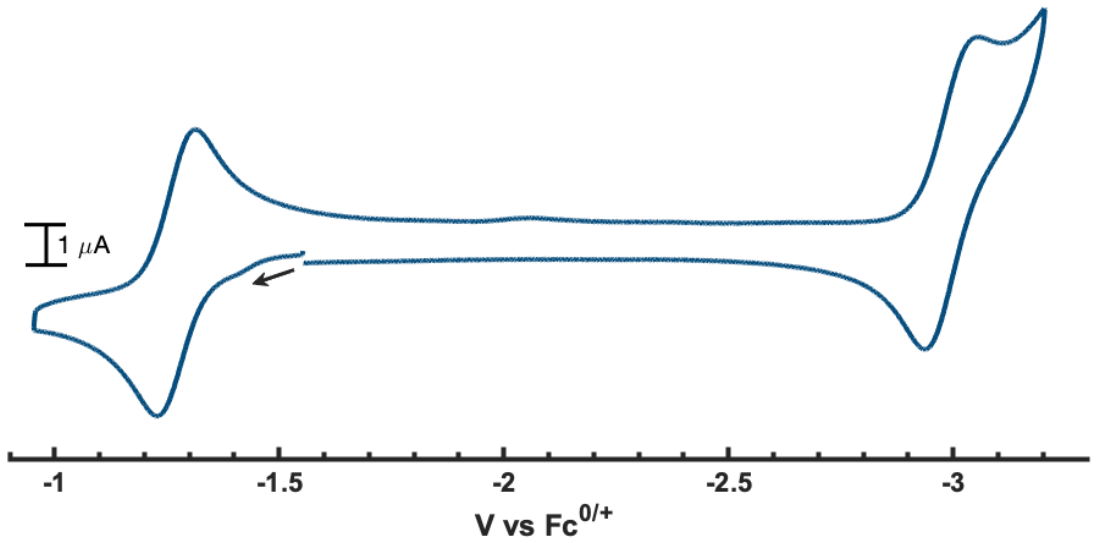

Figure S28: Cyclic voltammogram of **1**. Conditions: 4 mM **1** in THF under Ar, 0.4 M TBA PF_6, 200 mV/s scan rate.

Table S5: Comparison of the electrochemical $[NiML]^{0/+}$ and $[NiML]^{-/0}$ redox potentials (V vs. $Fc^{+/0}$) and ^{31}P NMR shifts (ppm) of $NiLH_3$, **1**, **2**, **3**, and **4** in THF.

	$NiLH_3$	1	2	3	4
$[NiML]^{0/+}$	−1.02	–1.26	−0.74	−0.57	Ca. −0.39*
$[NiML]^{0/-}$	N/A	–3.00	−2.82	−2.48	−2.34**
^{31}P δ	30.2	17.5	31.6	37.6	44.4

*Irreversible oxidation, i_{pa} used as a proxy. **Quasi-reversible.

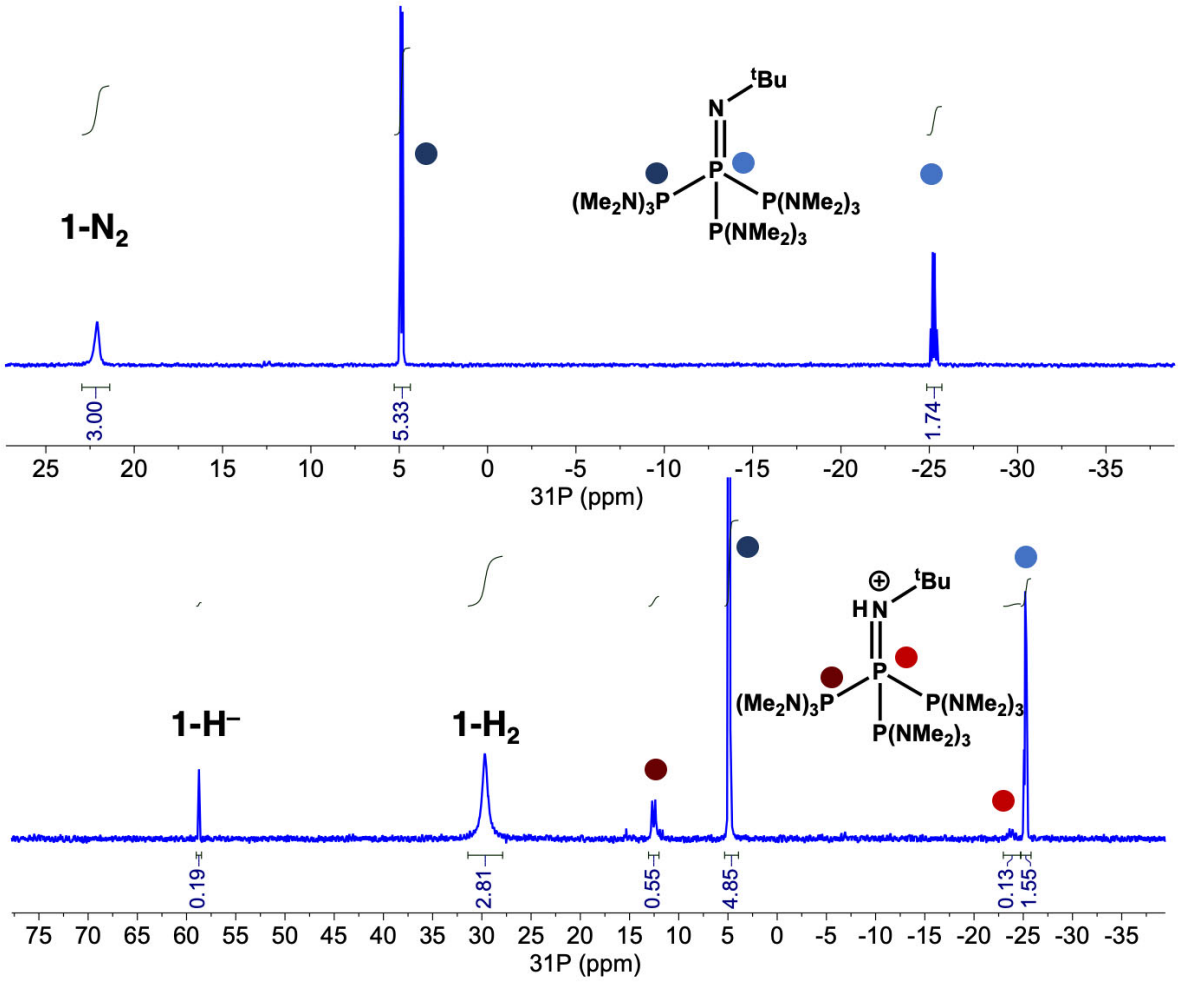

Figure S29: A representative example of the H_2 heterolysis reaction of **1-H₂** and $P_4{}^tBu$ in THF-d_8 starting from **1-N₂** before (top) and after the addition of 1 atm H_2 (bottom), as monitored by ^{31}P NMR spectroscopy.

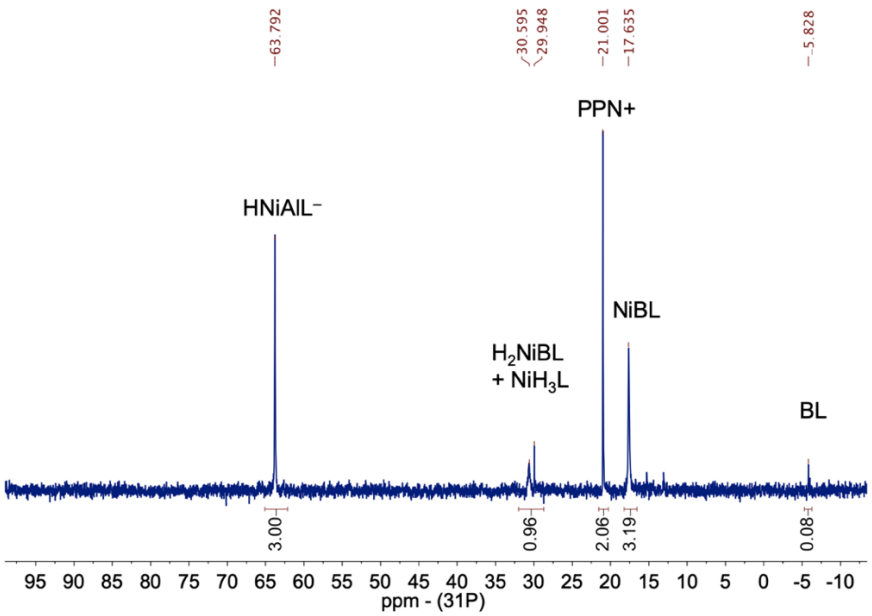

Figure S30: The observed reaction of **1** and [PPN][**2-H**$^-$] in THF-d_8 over the span of three days resulting in no production of **1-H**$^-$. After 3 days, some decomposition to BL, NiH_3L, and H_2 (trapped as (H_2)NiBL) was observed. PPN = bis(triphenylphosphine)iminium cation

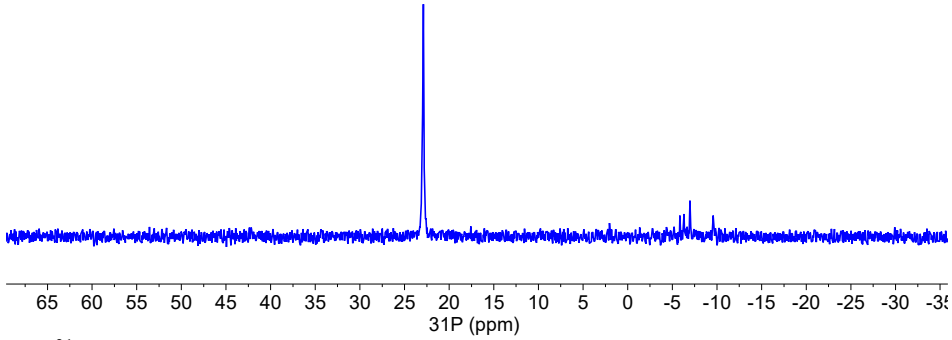

Figure S31: The ^{31}P NMR spectra of the reaction of **1-N$_2$** and 1 equiv NaHB^{s}Bu$_3$ in THF-d_8. Note the signal of **1-N$_2$** at 23 ppm and the lack of signal of **1-H**$^-$ indicate a lack of reactivity**.** The signals observed ~ –5 ppm are likely attributable to the reaction of NaHB^{s}Bu with a minor impurity of BL decomposition.

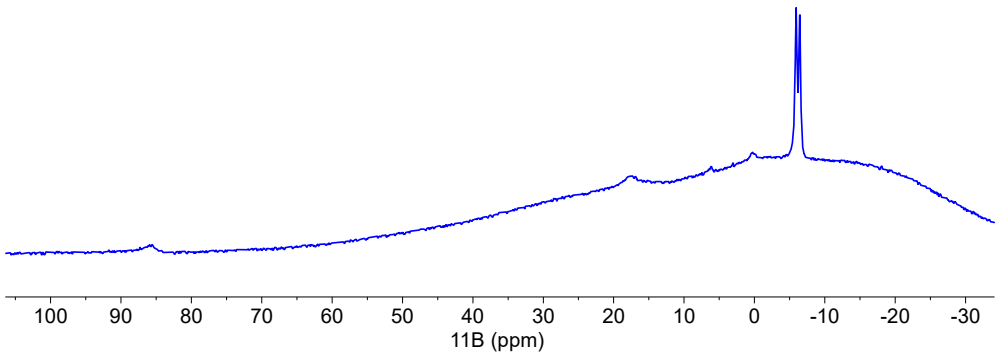

Figure S32: The ^{1}H NMR spectra of the reaction of **1-N$_2$** and **1** equiv NaHB^{s}Bu$_3$ in THF-d$_8$. The signals at ~18 ppm and –8 ppm are attributable to **1-N$_2$** and NaHB^{s}Bu$_3$, respectively. The other signals are likely the result to the reaction of NaHB^{s}Bu with a minor impurity of BL.

Calculation of the Thermodynamic Hydricity and Bond Dissociation Free Energy Values

Using the method of the combination of H_2 addition equilibria, pK_a(H_2) measurement, and the H_2 self-heterolysis constant, the thermodynamic hydricity, $\Delta G°_{H^-}$, of **1-H**$^-$ was determined.[15] For $\Delta G°_{H^-}$ (THF) the binding equilibria of **1-H$_2$**; pK_a equilibria and **1-H$_2$**, **1-H**$^-$, phosphazene/-ium; and H_2 self-heterolysis were all measured in THF, so that only THF values were used for consistency.[16,17] Literature acetonitrile values were used for phosphazene pK_a and the H_2 self-heterolysis constant to yield an expected thermodynamic hydricity for **1-H**$^-$ in acetonitrile.[15,16]

$$(H_2)M \rightleftharpoons H_2 + M \qquad \Delta G° = -1.364\log(K_1) \qquad \textbf{(S1)}$$

$$MH^- + HB^+ \rightleftharpoons (H_2)M + B \qquad \Delta G° = -1.364\log(K_2) \qquad \textbf{(S2)}$$

$$H^+ + B \rightleftharpoons HB^+ \qquad \Delta G° = -1.364(pK_a) \qquad \textbf{(S3)}$$

$$H_2 \rightleftharpoons H^+ + H^- \qquad \Delta G° = 68.7_{(THF)}\ \text{kcal/mol} \qquad \textbf{(S4)}$$

$$MH^- \rightleftharpoons M + H^- \qquad \Delta G°_{H^-} \qquad \textbf{(S5)}$$

Table S6: The values used for the determination of $\Delta G°_{H^-}$.

Value	THF	CH_3CN
inverse of H_2 binding (K_1)	0.0449	*0.0449**
inverse of proton transfer from Ni-H_2 to $P_4{}^tBu$ (K_2)	127.3	*127.3**
$P_4{}^tBu$ pK_a	33.9	42.7
H_2 self-heterolysis (kcal/mol)	68.7	76.0
$\Delta G°_{H^-}$	21.4 kcal/mol	16.7 kcal/mol

*measured in THF, presumed to be similar in CH_3CN

Table S7: The values used for the determination of BDFE for **1-H**$^-$. Note due to the insolubility of **1** in acetonitrile, its reduction potential in THF is used as a proxy: we have previously observed a minimal change in the potentials for the **2**, **3**, and **4** when changing between THF and acetonitrile. The value for $E°_{1/2}$ $H^-/H^\bullet$ (THF) was determined by combining the values of C_G(THF)[18] and $\Delta G°_{H^+/H^-}$(THF)[17].

Value	THF	CH_3CN
$E°_{1/2}$ (V vs Fc/Fc^+)	–3.00	*–3.00**
$\Delta G°_{H^-}$ (kcal/mol)	21.4	16.7
$E°_{1/2}$ $H^-/H^\bullet$ (kcal/mol vs Fc/Fc^+)	–23.9	–26.0[15]
BDFE (kcal/mol)	64.6 kcal/mol	59.9 kcal/mol

*measured in THF, presumed to be similar in CH_3CN

$$M + e^- \rightleftharpoons M^- \qquad \Delta G° = -23.06(E°_{1/2})$$

$$MH^- \rightleftharpoons M + H^- \qquad \Delta G°_{H-}$$

$$H^- \rightleftharpoons H^\bullet + e^- \qquad \Delta G° = -23.9_{\ (THF)} / -26.0_{(MeCN)}\ \text{kcal/mol}$$

$$MH^- \rightleftharpoons M^- + H^\bullet \qquad \text{BDFE}$$

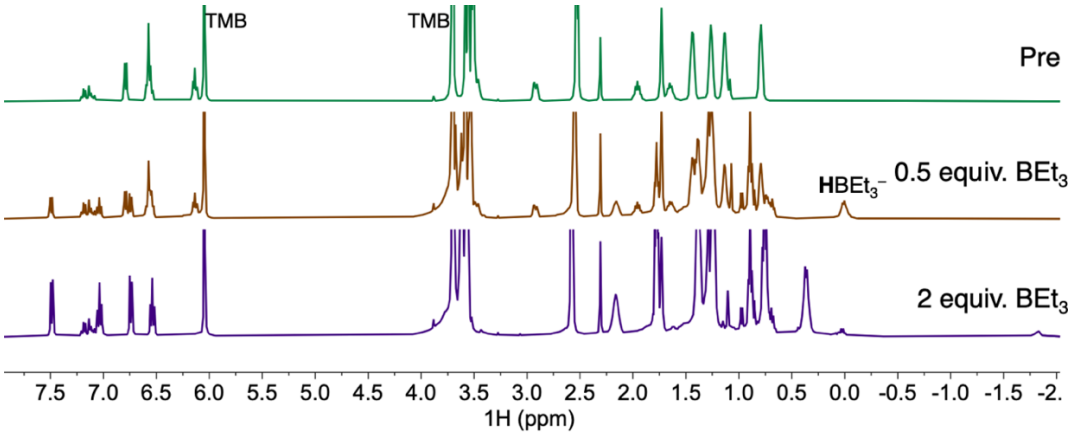

Figure S33: The ^{1}H NMR spectra (400 MHz) monitoring the reaction of **1-H**$^{-}$ and BEt_3 in THF-d_8 under Ar with 1,3,5-trimethoxybenzene (abbrev. TMB) as an internal standard. Each spectrum was taken within ten minutes of addition of reagent. Upon addition of excess BEt_3 the hydridic signal for $HBEt_3^-$ is diminished and a new signal at –1.8 ppm as well as at 0.3 and 0.76 ppm corresponding to new ethyl moieties.

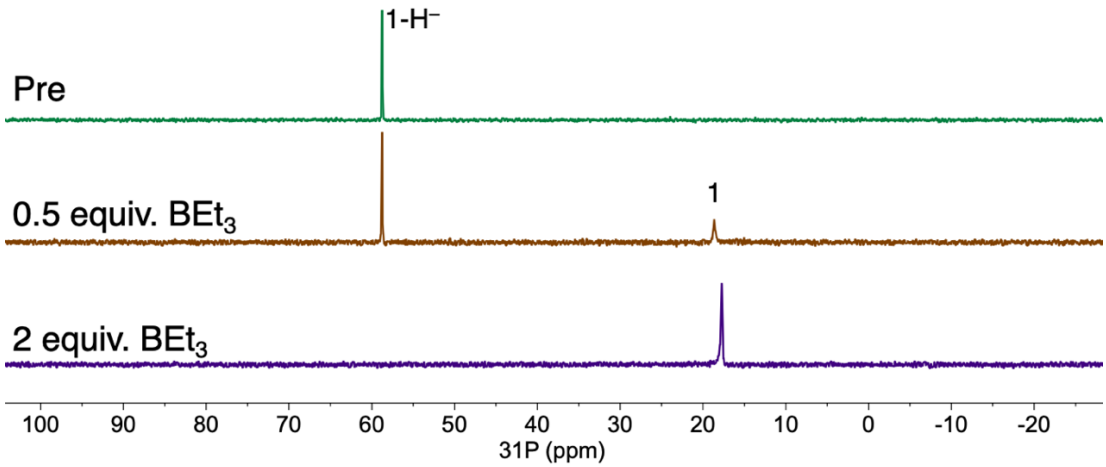

Figure S34: The ^{31}P NMR spectra (162 MHz) monitoring the reaction of **1-H**$^{-}$ and BEt_3 in THF-d_8. Each spectrum was taken within ten minutes of addition of reagent.

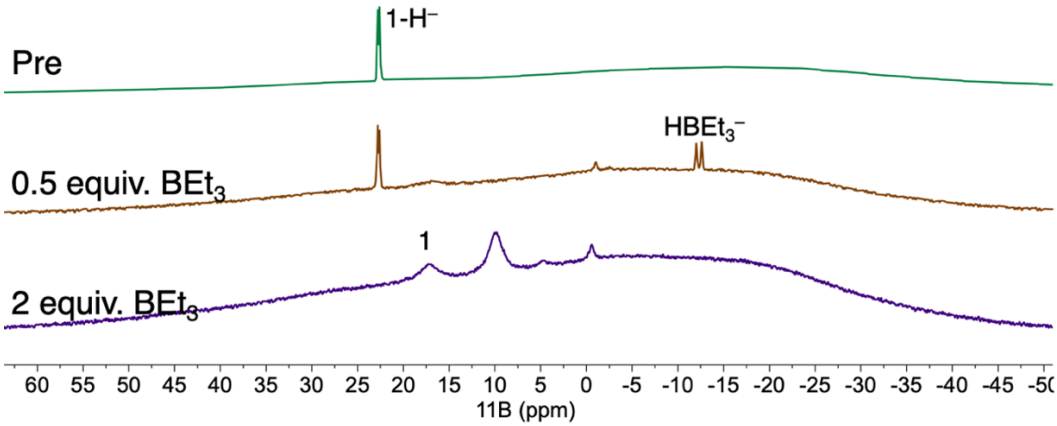

Figure S35: The ^{11}B NMR spectra (128 MHz) monitoring the reaction of **1-H**$^{-}$ and BEt_3 in THF-d_8. Each spectrum was taken within ten minutes of addition of reagent. The signal at –0.1 is a currently unknown minor impurity in the neat BEt_3 reagent. The signal at ca. 9 ppm is currently an unknown byproduct of the reaction with excess BEt_3. Others have noted the combination of BEt_3 and $HBEt_3^-$ has potential for the

formation of BEt_3 adducts[19] or to disproportionate to other products[20]. This signal does not correspond to known products from these reactions in the literature. It is clear that the addition of excess BEt_3 results in the consumption of **1-H**$^-$ (with production of **1**) as well as the loss of the signal for $HBEt_3$.

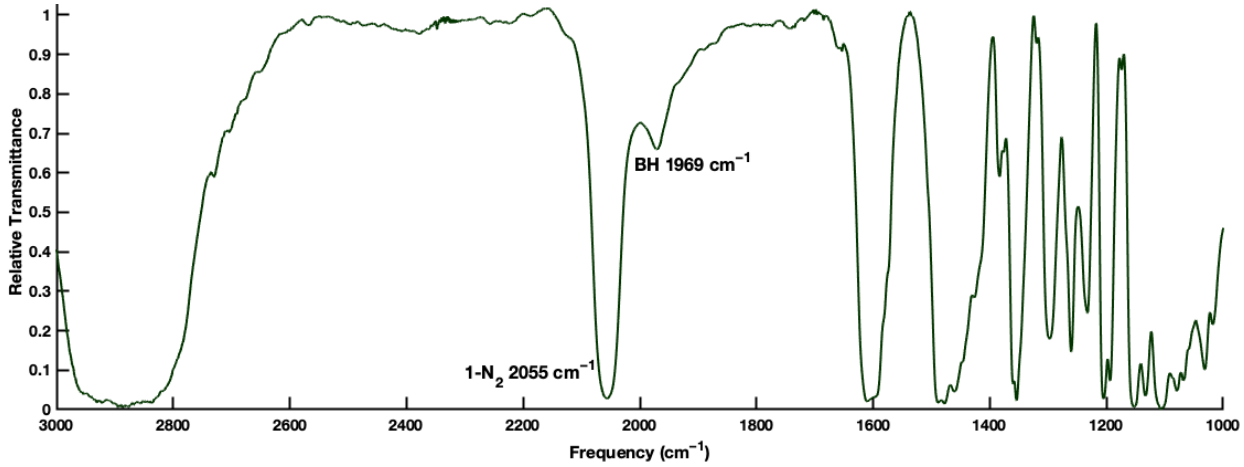

Figure S36: IR spectrum (KBr pellet) post-reaction of **1-H**$^-$ and 2 equiv. BEt_3 after the NMR sample was brought into an N_2 glovebox and volatiles were removed. Signals attributable to **1-N$_2$** and the $HBEt_3^-$ anion are apparent at 2055 cm^{-1} and 1969 cm^{-1} respectively.[21]

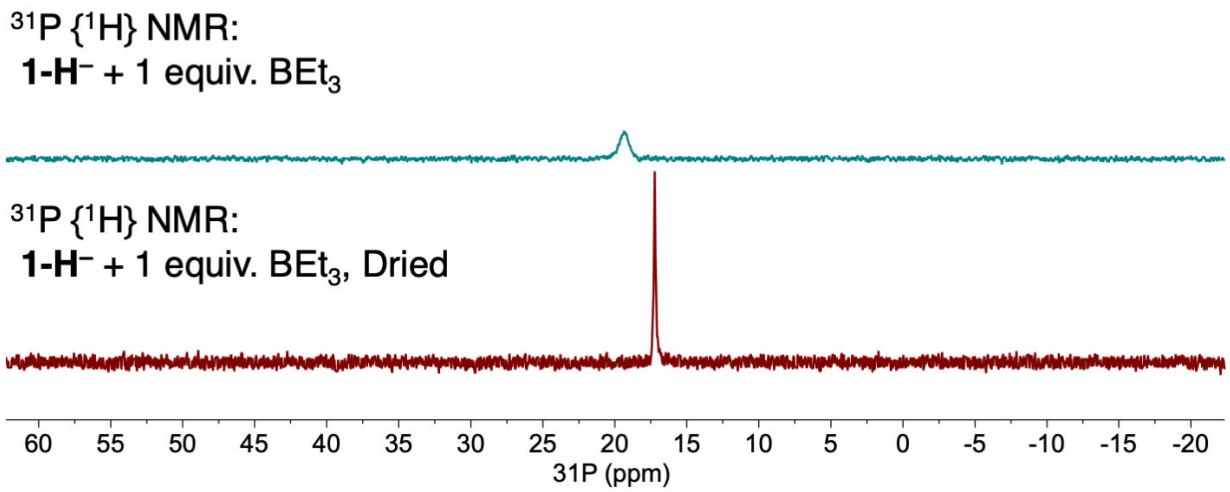

Figure S37: (Top) The $^{31}P\{^{1}H\}$ NMR spectrum (162 MHz) of the reaction of **1-H**$^{-}$ and 1 equiv. BEt_3 in THF-d_8 under Ar, taken ca. ten minutes after addition of borane. (Bottom) The $^{31}P\{^{1}H\}$ NMR spectrum of the dried and reconstituted (THF-d_8, Ar) reaction of **1-H**$^{-}$ and 1 equiv. BEt_3. Both spectra are consistent with **1** as the only metal product.

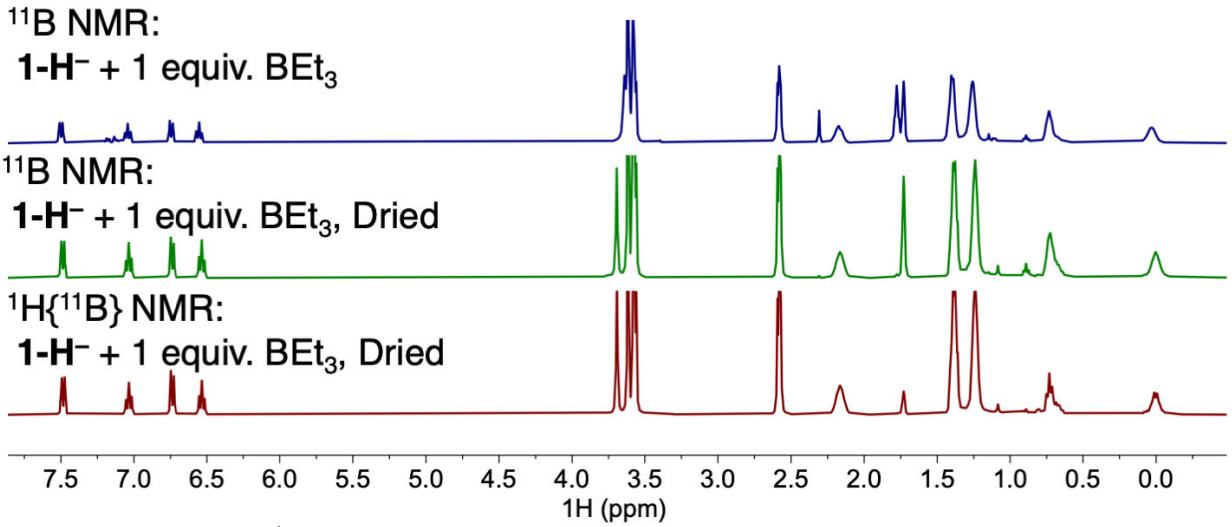

Figure S38: (Top) The ^{1}H NMR spectrum (400 MHz) of the reaction of **1-H**$^{-}$ and 1 equiv. BEt_3 in THF-d_8 under Ar, taken ca. ten minutes after addition of borane. (Middle) The ^{1}H NMR spectrum of the dried and reconstituted (THF-d_8, Ar) reaction of **1-H**$^{-}$ and 1 equiv. BEt_3. (Bottom) The $^{1}H\{^{11}B\}$ NMR spectrum of the dried and reconstituted (THF-d8, Ar) reaction of **1-H**$^{-}$ and 1 equiv. BEt_3. Note the signal for the anionic $HBEt_3^{-}$ product is observable at ca. 0.0 ppm.

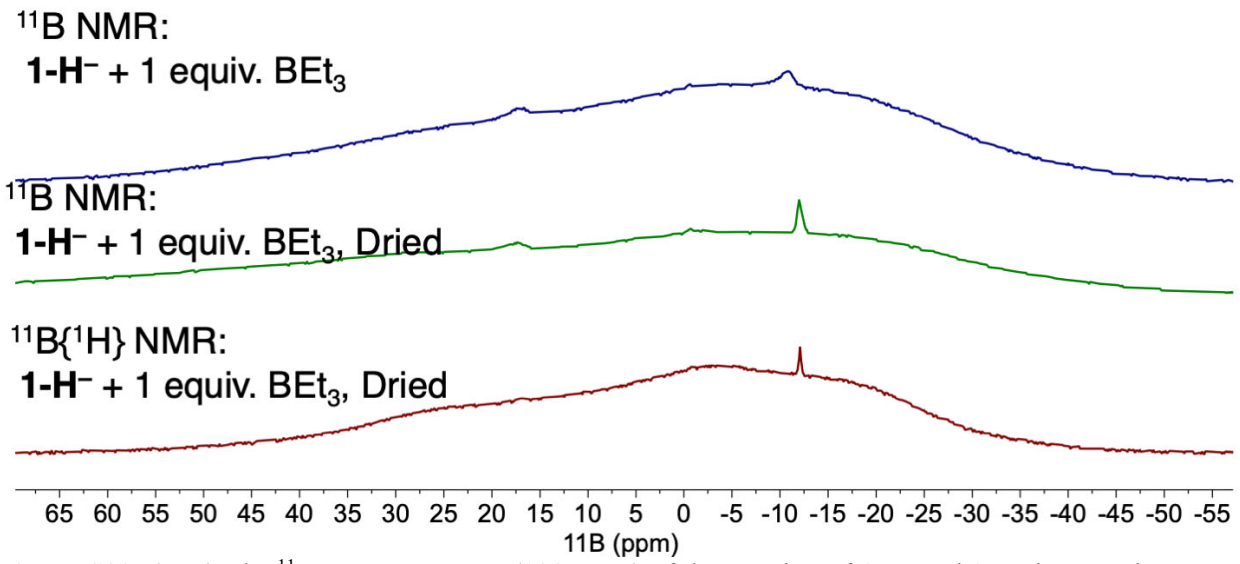

Figure S39: (Top) The ^{11}B NMR spectrum (128 MHz) of the reaction of **1-H**$^-$ and 1 equiv. BEt_3 in THF-d_8 under Ar, taken ca. ten minutes after addition of borane. (Middle) The ^{11}B NMR spectrum of the dried and reconstituted (THF-d_8, Ar) reaction of **1-H**$^-$ and 1 equiv. BEt_3. (Bottom) The ^{11}B{^{1}H} NMR spectrum of the dried and reconstituted (THF-d_8, Ar) reaction of **1-H**$^-$ and 1 equiv. BEt_3. Note the signal for the anionic $HBEt_3^-$ product is observable at ca. 11 ppm. Unfortunately, the ^{1}H coupling of the hydride was not well resolved.

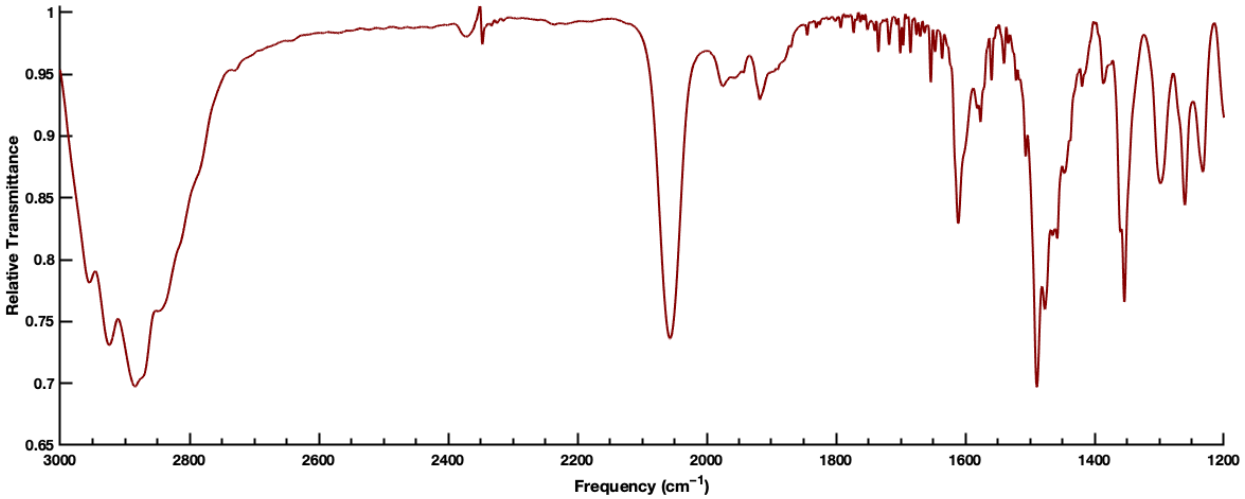

Figure S40: IR spectrum (KBr pellet) post-reaction of **1-H**$^-$ and 1 equiv. BEt_3 after the NMR sample was dried brought into an N_2 glovebox and volatiles were removed. Signals attributable to **1-N$_2$** and the $HBEt_3^-$ anion are apparent at 2055 cm^{-1} and 1969 cm^{-1} respectively.[21]

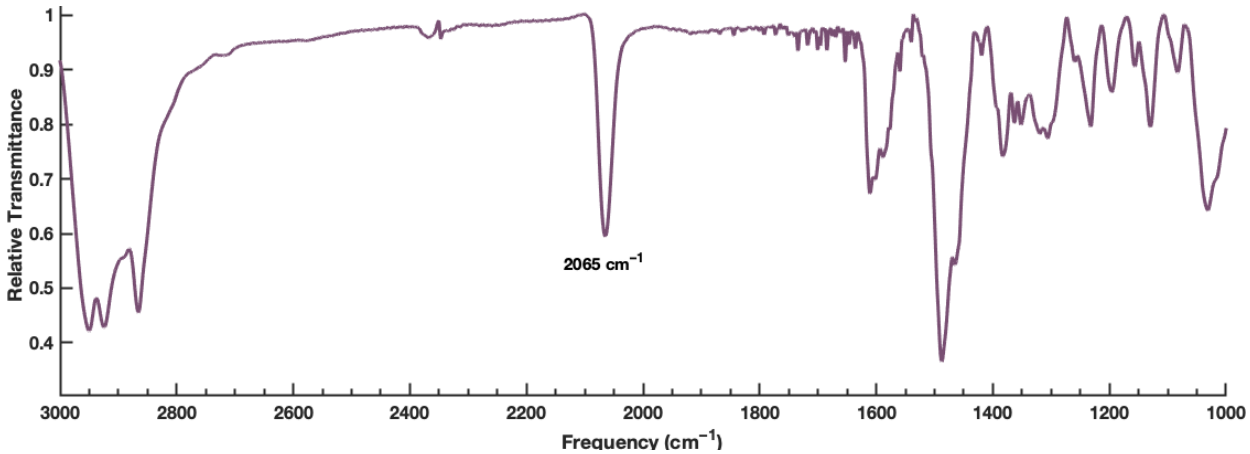

Figure S41: IR spectrum of **1-N$_2$.** (KBr pellet).

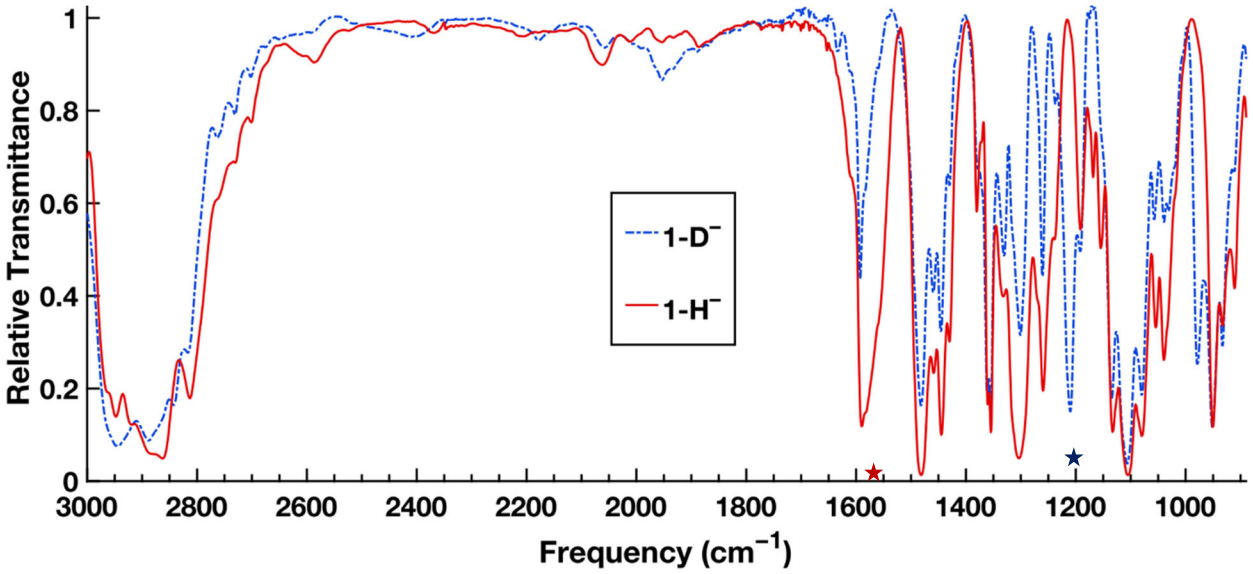

Figure S42: Comparison of IR spectra of crystalline samples **1-H$^-$** (red) and **1-D$^-$** (blue). (KBr pellet). The stretch observed at ca. 1600 cm^{-1} is tentatively assigned to the Ni-H stretch for **1-H$^-$** and the Ni-D stretch of **1-D$^-$** red shifts to 1210 cm^{-1} (as marked by stars).

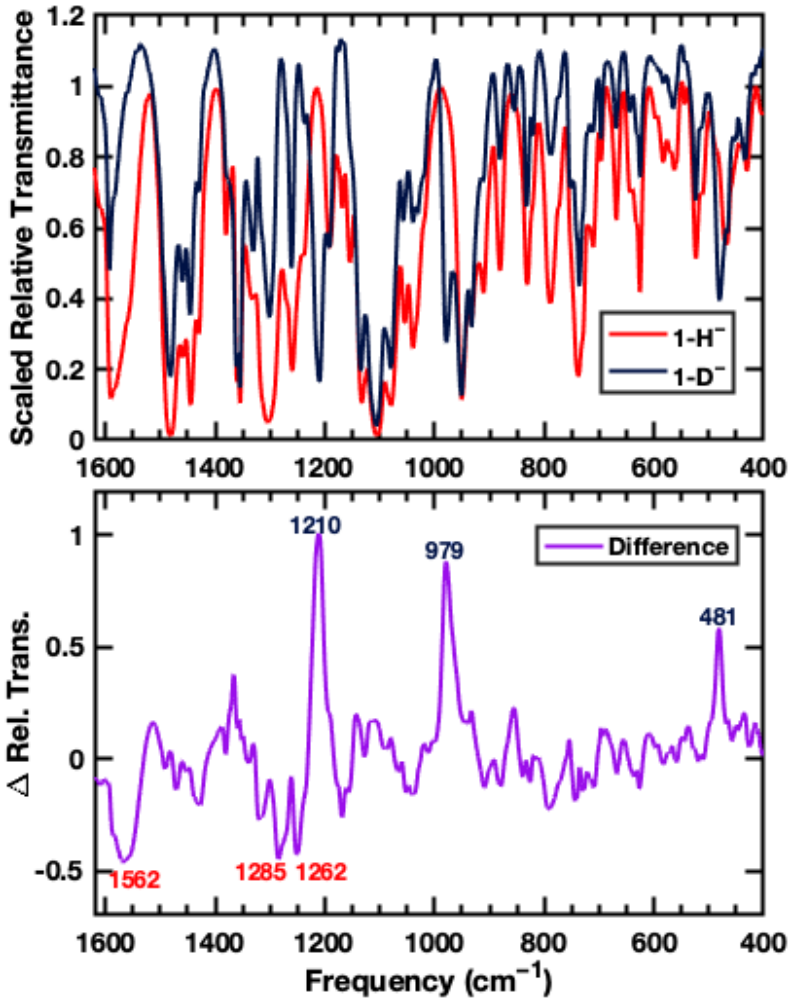

Figure S43: Top: the hydride and fingerprint region of IR spectra of **1-H**$^-$ and **1-D**$^-$ scaled to match intensities. Bottom: The difference spectrum between **1-H**$^-$ and **1-D**$^-$ to highlight any changes as the result of deuteration. Note, an ideal harmonic oscillator estimation would shift a Ni-H stretch of ~1565 cm^{-1} to ~1114 cm^{-1} upon deuteration (actual 1210 cm^{-1}).

Table S8: Collected thermodynamic values for **1**, **2**, **3**, and **4**.[22,23] Blue (left) boxes represent N_2 adducts, white (middle left) represent H_2 adducts, green (middle right) boxes represent the "naked" complexes, and the pink (right) boxes represent the anionic hydride adducts of the complexes.

M	$\Delta H°_{N_2}$ Tol.	$\Delta S°_{N_2}$ Tol.	$\Delta G°_{N_2}$ Tol.	$\Delta H°_{H_2}$ THF	$\Delta S°_{H_2}$ THF	$\Delta G°_{H_2}$ THF	$\Delta H°_{H_2}$ Tol.	$\Delta S°_{H_2}$ Tol.	$\Delta G°_{H_2}$ Tol.	pK_a H_2 THF	pK_a H_2 MeCN	$E°_{1/2}{}^{0/-}$ THF	$E°_{1/2}{}^{0/+}$ THF
B[d] (**1**)	–10.9(9)	–27(2)	–2.8(9)	–9.1(9)	–24(3)	–1.8(9)	–11.9(5)	–32(1)	–2.4(5)	37.4(2)	44.6(2)	–3.00	–1.26
Al (**2**)	–4.7(2)[a]	–27.5(5)[a]	3.5(3)[a]	–	–	–	–6.3(1)[a]	–26.4(4)[a]	1.6(2)[a]	28.6(1)[b]	36.7(1)[b]	–2.82[a]	−0.74[a]
Ga (**3**)	–4.7(3)[c]	–23(1)[c]	2.1(5)[c]	–7.5(1)[c]	–25.4(5)[c]	0.1(1)[c]	–6.3(1)[c]	–23.0(7)[c]	0.6(2)[c]	25.3(3)[c]	33.1(3)[c]	–2.48[c]	−0.57[c]
In (**4**)	–14.5(3)[a]	–45(1)[a]	–1.2(4)[a]	–	–	–	–14.8(6)[a]	–37(2)[a]	–3.0(7)[a]	24.1(1)[a]	31.9(1)[a]	–2.34[a]	Ca. −0.39[a]

Free energies and enthalpies are given in kcal/mol, entropies are given in cal/mol•K, and electrochemical values are given in V vs. the ferrocene/ferrocenium couple. Except for the N_2 and H_2 binding studies done in toluene, all solution-state values were obtained in THF. The p*K*a and thermodynamic hydricity values in acetonitrile were extrapolated using the methods for phosphazene bases and metal complexes described in references 16 and 24, respectively. Electrochemical values for **1** were not able to be obtained in acetonitrile due to the compound's insolubility in the solvent. However, as previously noted with **2-4**, the change in potentials between acetonitrile and THF is likely less than 100mV.[12] a**)** Cammarota, R. C. *et al. Chem. Sci.* **2019**,*10* (29), 7029–7042. b) Vollmer, M. V. Exploring Small Molecule Reactivity with Low-Valent Nickel and Cobalt Complexes Supported by Lewis Acidic Metalloligands, University of Minnesota, Minneapolis, Minnesota, U.S.A., 2019. c) Cammarota, R. C. *et al. J. Am. Chem. Soc.* **2017**, *139* (40), 14244–14250. d) This work.

Table S9: Collected thermodynamic values for **1-H**$^-$, **2-H**$^-$, **3-H**$^-$, and **4-H**$^-$.[22,23]

M	$\Delta G°_{H^-}$ THF	$\Delta G°_{H^-}$ MeCN	BDFE THF	BDFE MeCN	ν_{Ni-H}
B[d] (**1**)	21.4(9)	16.7(9)	66.7	59.9	1562
Al (**2**)	31.8(1)[b]	26.2(1)[b]	72.9[b]	64.9[b]	1646[b]
Ga (**3**)	34.7(5)[c]	31.3(5)[c]	58.6[b]	62.5[b]	1696[c]
In (**4**)	39.2(2)[b]	37.5(2)[b]	62.0[b]	65.5[b]	1714[b]

Free energies are given in kcal/mol and stretching frequencies are given in cm^{-1}. All solution state values were obtained in THF. Thermodynamic hydricity values in acetonitrile were extrapolated using the methods for metal complexes described in reference 24. a**)** Cammarota, R. C. *et al. Chem. Sci.* **2019**,*10* (29), 7029–7042. b) Vollmer, M. V. Exploring Small Molecule Reactivity with Low-Valent Nickel and Cobalt Complexes Supported by Lewis Acidic Metalloligands, University of Minnesota, Minneapolis, Minnesota, U.S.A., 2019. c) Cammarota, R. C. *et al. J. Am. Chem. Soc.* **2017**, *139* (40), 14244–14250. d) This work.

Computational Details

Density functional theory (DFT) calculations were performed with Gaussian 09 software.[29] Geometries were optimized in the gas phase with the M06-L functional and the following basis sets: def2- TZVPP for Ni; def2-TZVP for N, P, B, and O; def2-SVP basis set for any invariant C and H atoms.[30] The M06-L functional[31] and the above basis sets gave the best match to the experimental geometries. Structures were visualized using Chemcraft.[32] Harmonic vibrational frequencies were computed and confirmed the nature of all optimized structures (no imaginary frequencies).

Table S10: Selected bond lengths (Å) and angles (°) for optimized structure **1-H$^-$** and its corresponding experimental crystal structure. Differences in bond lengths and angles between the charged and neutral species are reported for both theory and experiment.

Parameter	**1-H$^-$**		
(Å, °, or cm^{-1})	**Exp.**	**M06-L**	**Diff** (Exp. – M06-L)
Ni–B	2.235(2)	2.235	0.003
r^b	1.07	1.07	0
Ni–H	1.56(2)	1.582	–0.02
Ni–P	2.1451(5)[a]	2.154[a]	–0.009
B–N_{Amide}	1.576(3)[a]	1.577[a]	–0.001
B–N_{Apical}	2.803(5)	2.770	0.03
∠P–Ni–P	117.97(3)[a]	117.4[a]	0.57
∠N_{Eq}–B–N_{Eq}	112.03(3)[a]	112.0[a]	0.03
∑(∡P−Ni−P)	354.0(3)	352.3	1.7
∑(∡N_{eq}−B−N_{eq})	336.08(2)	336.0	0.08
ν_{Ni-H}	1562	1558	4

[a]Average of three unique values. [b]Ratio of the Ni–B bond length to the sum of Ni and B covalent radii.

Table S1: Selected bond lengths (Å) and angles (°) for optimized structure **1** and its corresponding experimental crystal structure. Differences in bond lengths and angles between the charged and neutral species are reported for both theory and experiment.

Parameter	**1**		
(Å or °)	**Exp.**[b]	**M06-L**	**Diff** (Exp. – M06-L)
Ni–B	3.380(4)	3.348	0.03
Ni–P	2.1381(5)	2.142[a]	–0.004
B–N_{Amide}	1.5322(2)	1.532[a]	–0.0002
B–N_{Apical}	1.702(4)	1.692	0.01
∠P–Ni–P	117.251(9)	117.3[a]	–0.05
∠N_{Eq}–B–N_{Eq}	117.26(7)	117.6[a]	–0.34
∑(∡P–Ni–P)	351.75(9)	351.9	–0.40
∑(∡N_{eq}–B–N_{eq})	351.78(7)	352.8	–1.02

[a]Average of three unique values. [b]Trigonal space groups only display one value by symmetry.

Table S11: Selected bond lengths (Å) and angles (°) for optimized structure **1-N_2** and its corresponding experimental crystal structures Differences in bond lengths and angles between the charged and neutral species are reported for both theory and experiment.

Parameter	**1-N_2**		
(Å or °)	**Exp.**	**M06-L**	**Diff** (Exp. – M06-L)
Ni–B	3.735(2)	3.703	0.003
Ni–N_2	1.820(9)	1.847	–0.03
N–N	1.116(5)	1.120	–0.004
Ni–P	2.2065(5)[a]	2.219[a]	–0.001
B–N_{Amide}	1.527(6)[a]	1.519[a]	–0.001
B–N_{Apical}	1.682(3)	1.700	–0.02
∠P–Ni–P	109.67(4)[a]	109.7[a]	–0.03
∠N_{Eq}–B–N_{Eq}	117.06(3)[a]	117.4[a]	–0.34
∑(∡P−Ni−P)	329.01(4)	329.2	–0.19
∑(∡N_{eq}−B−N_{eq})	351.19(3)	352.2	–1.01

[a]Average of three unique values.

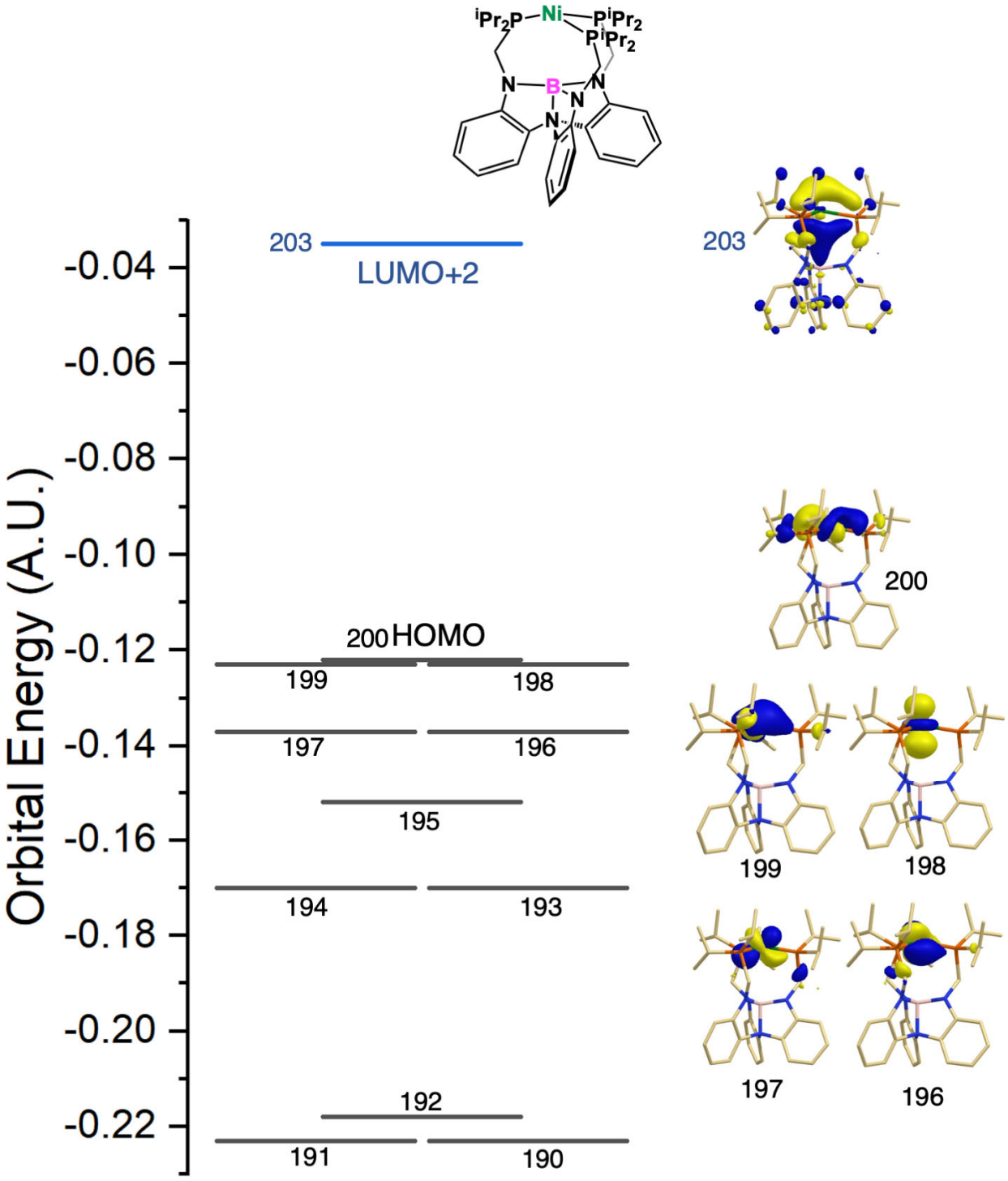

Figure S44: Kohn-Sham Orbitals of **1**, plotted at an isovalue of 0.05.

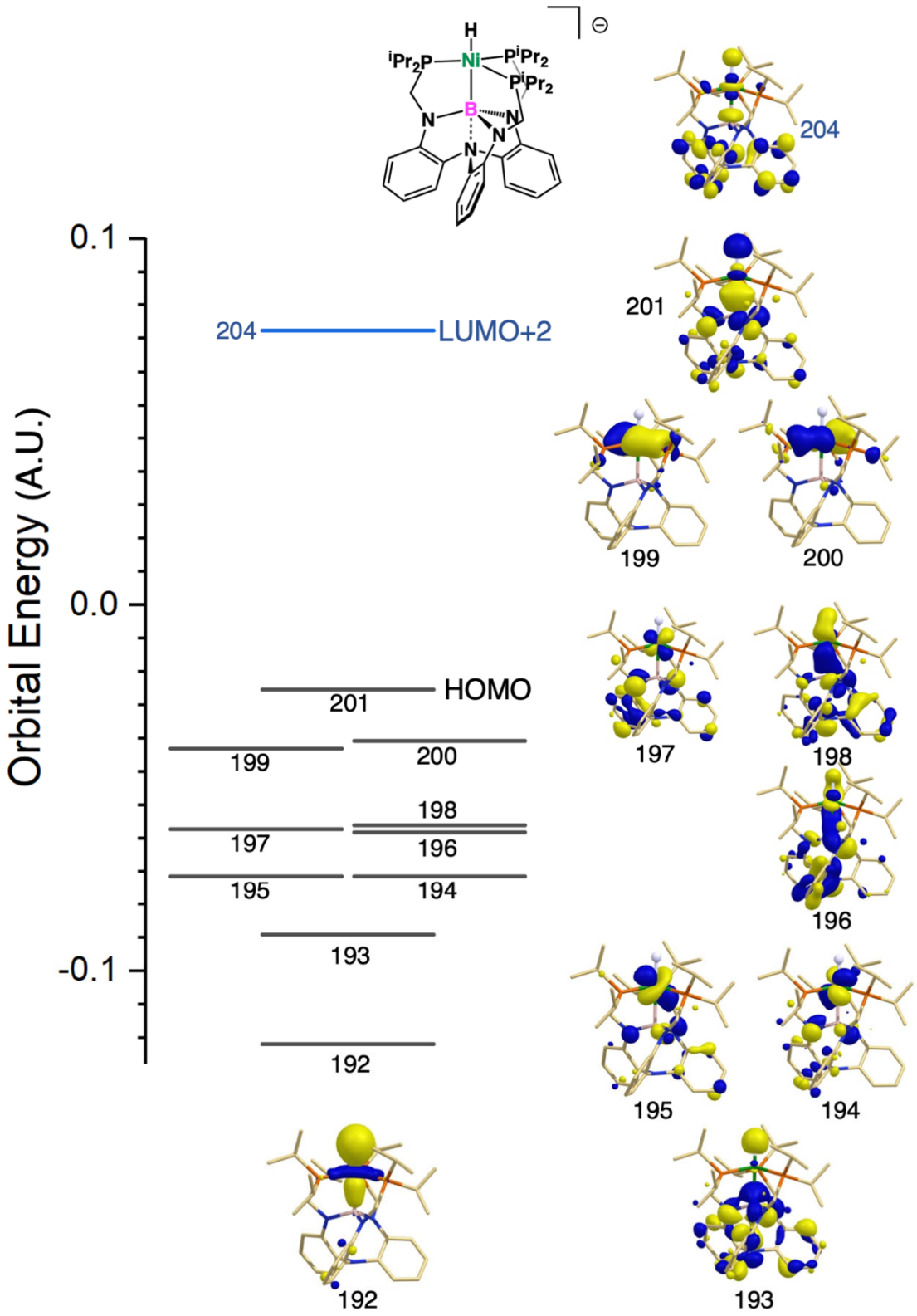

Figure S45: Kohn-Sham Orbitals of **1-H**$^{-}$, plotted at an isovalue of 0.05. The three MOs related to the 3-center (H-Ni-B), 2-electron σ-bond are labeled as 192, 201, and 204. The energy of the optimized **1-H**$^{-}$ (-4298.1094375 Hartrees) is lower in energy than a hypothetical isomer where the Ni-B interaction is absent (-4298.0802393 Hartrees).

Table S12: The row-wise correlation matrix for various properties of **1, 2, 3,** and **4**; and their respective H_2 and hydride adducts.

	Shannon Ionic Radii (IV)	Oxidation Potential	Reduction Potential	ΔG_{H^-} THF	^{31}P Shift	pKa H_2 THF
Shannon Ionic Radii (IV)	1.0000	0.9978	0.9405	0.9987	0.9980	-0.9770
Oxidation Potential	0.9978	1.0000	0.9404	0.9997	0.9982	-0.9889
Reduction Potential	0.9405	0.9404	1.0000	0.9345	0.9571	-0.9192
ΔG_{H^-} THF	0.9987	0.9997	0.9345	1.0000	0.9975	-0.9863
^{31}P Shift	0.9980	0.9982	0.9571	0.9975	1.0000	-0.9820
pKa H_2 THF	-0.9770	-0.9889	-0.9192	-0.9863	-0.9820	1.0000

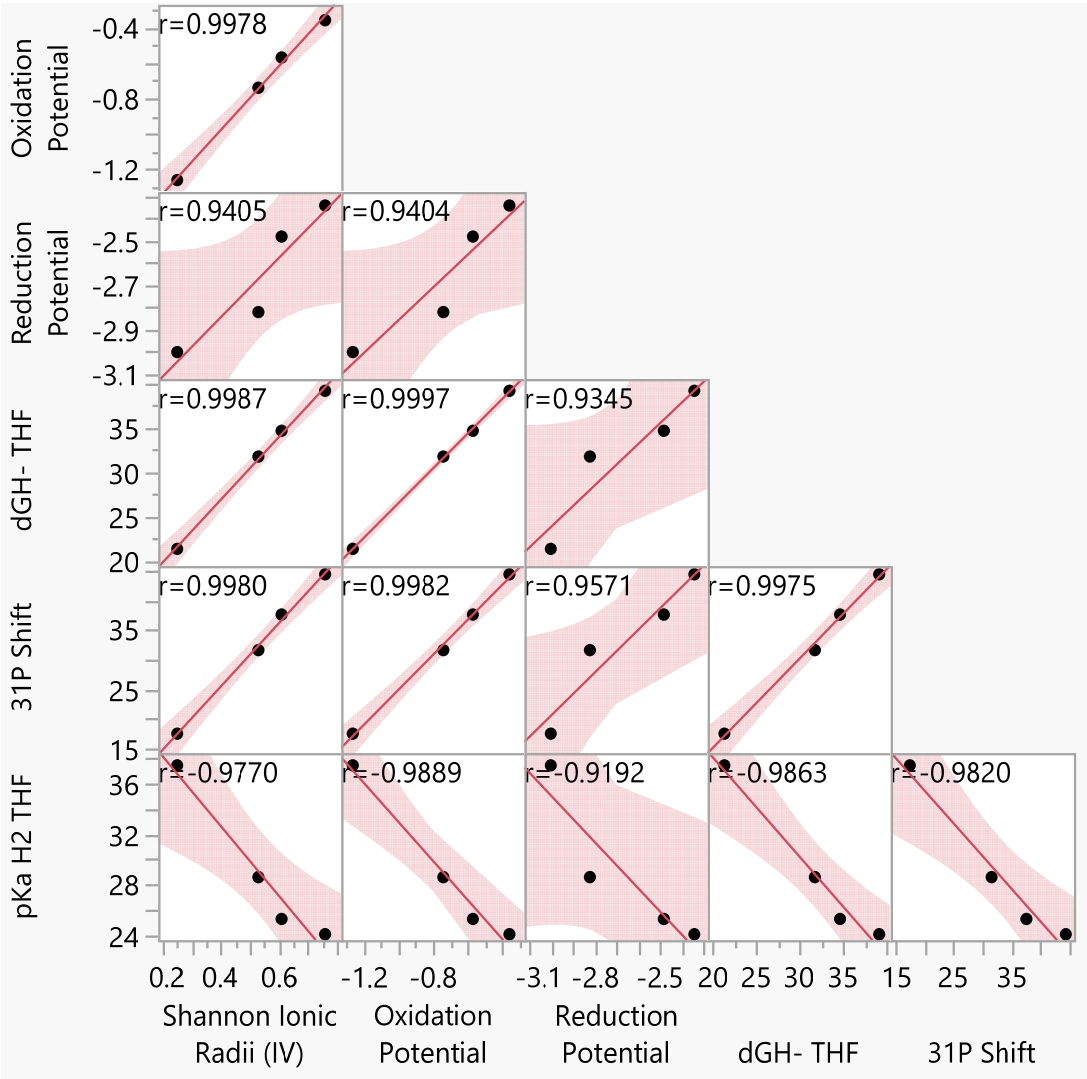

Figure S46: The scatterplot correlation matrix for various properties of **1, 2, 3,** and **4** used in Table S12.

Table S13: A comparison of the calculated enthalpy of hydride transfer values, literature thermodynamic hydricity values, the predicted hydricity values from a linear correlation between them (see Figure S47, below), and computationally predicted thermodynamic hydricity values. All values are in kcal/mol. [a]Values used from reference 25.

	R	Calc. ΔH_{H^-} MeCN[a]	Lit. ΔG_{H^-} MeCN[a]	Linear Correlation ΔG_{H^-}	Calculated ΔG_{H^-}[a]
$[BR_3H]^-$	O^{t}Bu	9.23		5.127	0.62
	$OSiMe_3$	15.41		10.79	5.01
	^{s}Bu	28.6		22.86	19.99
	Et	32.22	26	26.17	24.39
	Ph	42.22	36	35.33	44.55
	F	56.51		48.41	49.1
	H	58.15	50	49.91	50.45
	C_6F_5	71.18		61.84	64.95
AlH_4^-	–	50.82	43	43.20	42.56

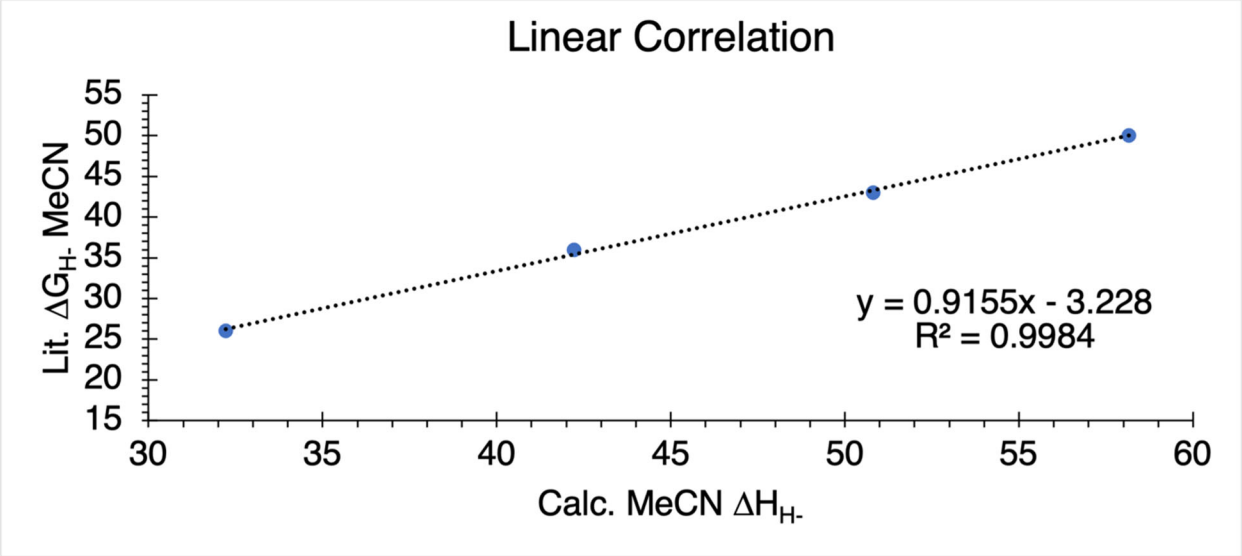

Figure S47: The plot between literature thermodynamic hydricity values and their respective computationally determined enthalpy of hydride transfer values. Values taken from reference 25. The produced equation allows for a semi-empirical method for interconverting calculated enthalpies of hydride transfer into predicted estimations of thermodynamic hydricities on the acetonitrile scale. Note the closer correlation to the literature values than the calculated thermodynamic hydricities enabling reasonable predictions at the extreme regimes.

References

(1) Rudd, P. A.; Liu, S.; Gagliardi, L.; Young, V. G.; Lu, C. C. Metal–Alane Adducts with Zero-Valent Nickel, Cobalt, and Iron. *J. Am. Chem. Soc.* **2011**, *133* (51), 20724–20727. https://doi.org/10.1021/ja2099744.

(2) Prat, J. R.; Gaggioli, C. A.; Cammarota, R. C.; Bill, E.; Gagliardi, L.; Lu, C. C. Bioinspired Nickel Complexes Supported by an Iron Metalloligand. *Inorg. Chem.* **2020**, *59* (19), 14251–14262. https://doi.org/10.1021/acs.inorgchem.0c02041.

(3) Blessing, R. H. An Empirical Correction for Absorption Anisotropy. *Acta Crystallogr. A* **1995**, *51* (1), 33–38. https://doi.org/10.1107/S0108767394005726.

(4) Sheldrick, G. M. *SHELXT* – Integrated Space-Group and Crystal-Structure Determination. *Acta Crystallogr. Sect. Found. Adv.* **2015**, *71* (1), 3–8. https://doi.org/10.1107/S2053273314026370.

(5) Hübschle, C. B.; Sheldrick, G. M.; Dittrich, B. *ShelXle* : A Qt Graphical User Interface for *SHELXL*. *J. Appl. Crystallogr.* **2011**, *44* (6), 1281–1284. https://doi.org/10.1107/S0021889811043202.

(6) Sheldrick, G. M. Crystal Structure Refinement with *SHELXL*. *Acta Crystallogr. Sect. C Struct. Chem.* **2015**, *71* (1), 3–8. https://doi.org/10.1107/S2053229614024218.

(7) Spek, A. L. Structure Validation in Chemical Crystallography. *Acta Crystallogr. D Biol. Crystallogr.* **2009**, *65* (2), 148–155. https://doi.org/10.1107/S090744490804362X.

(8) Kubas, G. J. Fundamentals of H2 Binding and Reactivity on Transition Metals Underlying Hydrogenase Function and H2 Production and Storage. *Chem. Rev.* **2007**, *107* (10), 4152–4205. https://doi.org/10.1021/cr050197j.

(9) Bautista, M. T.; Earl, K. A.; Maltby, P. A.; Morris, R. H.; Schweitzer, C. T.; Sella, Andrea. Estimation of the Hydrogen-Hydrogen Distances of .Eta.2-Dihydrogen Ligands in the Complexes Trans-[M(.Eta.2-H2)(H)(PR2CH2CH2PR2)2]+ [M = Iron, Ruthenium, R = Ph, M = Osmium, R = Et] by Solution NMR Methods. *J. Am. Chem. Soc.* **1988**, *110* (21), 7031–7036. https://doi.org/10.1021/ja00229a015.

(10) Morris, R. H.; Wittebort, R. J. Effect of a Libration or Hopping Motion of the H2-Dihydrogen Ligand on Longitudinal Nuclear Magnetic Resonance Relaxation. *Magn. Reson. Chem.* **1997**, *35* (4), 243–250. https://doi.org/10.1002/(SICI)1097-458X(199704)35:4<243::AID-OMR61>3.0.CO;2-S.

(11) Desrosiers, P. J.; Cai, L.; Lin, Z.; Richards, R.; Halpern, J. Assessment of the "T1 Criterion" for Distinguishing between Classical and Nonclassical Transition-Metal Hydrides: Hydride Relaxation Rates in Tris(Triarylphosphine)Osmium Tetrahydrides and Related Polyhydrides. *J. Am. Chem. Soc.* **1991**, *113* (11), 4173–4184. https://doi.org/10.1021/ja00011a019.

(12) Cammarota, R. C.; Xie, J.; Burgess, S. A.; Vollmer, M. V.; Vogiatzis, K. D.; Ye, J.; Linehan, J. C.; Appel, A. M.; Hoffmann, C.; Wang, X.; Young, V. G.; Lu, C. C. Thermodynamic and Kinetic Studies of H2 and N2 Binding to Bimetallic Nickel-Group 13 Complexes and Neutron Structure of a Ni(H2-H2) Adduct. *Chem. Sci.* **2019**, *10* (29), 7029–7042. https://doi.org/10.1039/C9SC02018G.

(13) Brunner, E. Solubility of Hydrogen in 10 Organic Solvents at 298.15, 323.15, and 373.15 K. *J. Chem. Eng. Data* **1985**, *30* (3), 269–273. https://doi.org/10.1021/je00041a010.

(14) Burgess, D. IUPAC/NIST Solubility Data Series, NIST Standard Reference Database 106, 2007. https://doi.org/10.18434/T4QC79.

(15) Wiedner, E. S.; Chambers, M. B.; Pitman, C. L.; Bullock, R. M.; Miller, A. J. M.; Appel, A. M. Thermodynamic Hydricity of Transition Metal Hydrides. *Chem. Rev.* **2016**, *116* (15), 8655–8692. https://doi.org/10.1021/acs.chemrev.6b00168.
(16) Saame, J.; Rodima, T.; Tshepelevitsh, S.; Kütt, A.; Kaljurand, I.; Haljasorg, T.; Koppel, I. A.; Leito, I. Experimental Basicities of Superbasic Phosphonium Ylides and Phosphazenes. *J. Org. Chem.* **2016**, *81* (17), 7349–7361. https://doi.org/10.1021/acs.joc.6b00872.
(17) Brereton, K. R.; Smith, N. E.; Hazari, N.; Miller, A. J. M. Thermodynamic and Kinetic Hydricity of Transition Metal Hydrides. *Chem. Soc. Rev.* **2020**, *49* (22), 7929–7948. https://doi.org/10.1039/D0CS00405G.
(18) Wise, C. F.; Agarwal, R. G.; Mayer, J. M. Determining Proton-Coupled Standard Potentials and X–H Bond Dissociation Free Energies in Nonaqueous Solvents Using Open-Circuit Potential Measurements. *J. Am. Chem. Soc.* **2020**, *142* (24), 10681–10691. https://doi.org/10.1021/jacs.0c01032.
(19) Mock, M. T.; Potter, R. G.; Camaioni, D. M.; Li, J.; Dougherty, W. G.; Kassel, W. S.; Twamley, B.; DuBois, D. L. Thermodynamic Studies and Hydride Transfer Reactions from a Rhodium Complex to BX_3 Compounds. *J. Am. Chem. Soc.* **2009**, *131* (40), 14454–14465. https://doi.org/10.1021/ja905287q.
(20) Crestani, M. G.; Muñoz-Hernández, M.; Arévalo, A.; Acosta-Ramírez, A.; García, J. J. σ-Borane Coordinated to Nickel(0) and Some Related Nickel(II) Trihydride Complexes. *J. Am. Chem. Soc.* **2005**, *127* (51), 18066–18073. https://doi.org/10.1021/ja056000m.
(21) Brown, H. C.; Kramer, G. W.; Hubbard, J. L.; Krishnamurthy, S. Addition Compounds of Alkali Metal Hydrides. *J. Organomet. Chem.* **1980**, *188* (1), 1–10. https://doi.org/10.1016/S0022-328X(00)83693-1.
(22) Cammarota, R. C. Greater than the Sum of Its Parts: Tuning Nickel for Uncommon Small Molecule Reactivity and Catalysis via Dative Bonds with Group 13 Lewis Acidic Metalloligands, University of Minnesota, Minneapolis, Minnesota, U.S.A., 2018.
(23) Vollmer, M. V. Exploring Small Molecule Reactivity with Low-Valent Nickel and Cobalt Complexes Supported by Lewis Acidic Metalloligands, University of Minnesota, Minneapolis, Minnesota, U.S.A., 2019.
(24) Vollmer, M. V.; Ye, J.; Linehan, J. C.; Graziano, B. J.; Preston, A.; Wiedner, E. S.; Lu, C. C. Cobalt-Group 13 Complexes Catalyze CO2 Hydrogenation via a Co(−I)/Co(I) Redox Cycle. *ACS Catal.* **2020**, *10* (4), 2459–2470. https://doi.org/10.1021/acscatal.9b03534.
(25) Heiden, Z. M.; Lathem, A. P. Establishing the Hydride Donor Abilities of Main Group Hydrides. *Organometallics* **2015**, *34* (10), 1818–1827. https://doi.org/10/f7fh7b.
(26) Yang, L.; Powell, D. R.; Houser, R. P. Structural Variation in Copper(I) Complexes with Pyridylmethylamide Ligands: Structural Analysis with a New Four-Coordinate Geometry Index, T4. *Dalton Trans.* **2007**, No. 9, 955–964. https://doi.org/10.1039/B617136B.
(27) Rosiak, D.; Okuniewski, A.; Chojnacki, J. Novel Complexes Possessing Hg–(Cl, Br, I)···OC Halogen Bonding and Unusual Hg2S2(Br/I)4 Kernel. The Usefulness of T4′ Structural Parameter. *Polyhedron* **2018**, *146*, 35–41. https://doi.org/10.1016/j.poly.2018.02.016.
(28) Okuniewski, A.; Rosiak, D.; Chojnacki, J.; Becker, B. Coordination Polymers and Molecular Structures among Complexes of Mercury(II) Halides with Selected 1-Benzoylthioureas. *Polyhedron* **2015**, *90*, 47–57. https://doi.org/10.1016/j.poly.2015.01.035.
(29) M. J. Frisch, G. W. Trucks, H. B. Schlegel, G. E. Scuseria, M. A. Robb, J. R. Cheeseman, G. Scalmani, V. Barone, G. A. Petersson, H. Nakatsuji, X. Li, M. Caricato, A. Marenich, J.

Bloino, B. G. Janesko, R. Gomperts, B. Mennucci, H. P. Hratchian, J. V. Ortiz, A. F. Izmaylov, J. L. Sonnenberg, D. Williams-Young, F. Ding, F. Lipparini, F. Egidi, J. Goings, B. Peng, A. Petrone, T. Henderson, D. Ranasinghe, V. G. Zakrzewski, J. Gao, N. Rega, G. Zheng, W. Liang, M. Hada, M. Ehara, K. Toyota, R. Fukuda, J. Hasegawa, M. Ishida, T. Nakajima, Y. Honda, O. Kitao, H. Nakai, T. Vreven, K. Throssell, J. A. Montgomery, Jr., J. E. Peralta, F. Ogliaro, M. Bearpark, J. J. Heyd, E. Brothers, K. N. Kudin, V. N. Staroverov, T. Keith, R. Kobayashi, J. Normand, K. Raghavachari, A. Rendell, J. C. Burant, S. S. Iyengar, J. Tomasi, M. Cossi, J. M. Millam, M. Klene, C. Adamo, R. Cammi, J. W. Ochterski, R. L. Martin, K. Morokuma, O. Farkas, J. B. Foresman, and D. J. Fox. *Gaussian 09, Revision A.02*; Gaussian, Inc.: Wallingford CT, 2016.

(30) Weigend, F.; Ahlrichs, R. Balanced Basis Sets of Split Valence, Triple Zeta Valence and Quadruple Zeta Valence Quality for H to Rn: Design and Assessment of Accuracy. *Phys. Chem. Chem. Phys.* **2005**, *7* (18), 3297–3305. https://doi.org/10.1039/B508541A.

(31) Zhao, Y.; Truhlar, D. G. A New Local Density Functional for Main-Group Thermochemistry, Transition Metal Bonding, Thermochemical Kinetics, and Noncovalent Interactions. *J. Chem. Phys.* **2006**, *125* (19), 194101. https://doi.org/10.1063/1.2370993.

(32) *Chemcraft - Graphical Software for Visualization of Quantum Chemistry Computations. https://www.chemcraftprog.com*.